Numerical simulations of the near wake of a sphere moving in a steady, horizontal motion through a linearly stratified fluid at Re = 1000

Trevor S. Orr, J. Andrzej Domaradzki, Geoffrey R. Spedding, and George S. Constantinescu

Citation: Physics of Fluids **27**, 035113 (2015); doi: 10.1063/1.4915139
View online: http://dx.doi.org/10.1063/1.4915139
View Table of Contents: http://scitation.aip.org/content/aip/journal/pof2/27/3?ver=pdfcov
Published by the AIP Publishing

PHYSICS OF FLUIDS **27**, 035113 (2015)

Numerical simulations of the near wake of a sphere moving in a steady, horizontal motion through a linearly stratified fluid at Re = 1000

Trevor S. Orr,[1,a)] J. Andrzej Domaradzki,[1,b)] Geoffrey R. Spedding,[1,c)] and George S. Constantinescu[2,d)]
[1]*Department of Aerospace and Mechanical Engineering, University of Southern California, Los Angeles, California 90089-1191, USA*
[2]*Department of Civil and Environmental Engineering, University of Iowa, Iowa City, Iowa 52242-1527, USA*

(Received 20 August 2014; accepted 11 February 2015; published online 24 March 2015)

A numerical investigation of the near wake of a sphere moving horizontally through a linearly stratified fluid is presented. Simulations are first performed on a flow with Reynolds number $Re = 200$ for a range of internal Froude number, $0.1 \leq Fr \leq \infty$. The simulations capture buoyant characteristic behavior, the presence of vortex shedding at low Fr, and lee waves. Simulations at higher Reynolds number, $Re = 1000$, for $1 \leq Fr \leq \infty$ provide a description and parametrization of the near wake, including the density field. At $Re = 1000$, the effects of utilizing two different averaging techniques in the unsteady near wake region are discussed. Perturbation quantities in the stratified near wake are anisotropic, and based on the oscillations of the centerline vertical perturbation velocity, the Fr at which the stratified near wake may be considered indistinguishable from the uniform density near wake is suggested to be $O(100)$. Parametrization of the near wake is accomplished using the parameterized vertical wake height, downstream distance from the sphere, and Fr as parameters. © *2015 AIP Publishing LLC.* [http://dx.doi.org/10.1063/1.4915139]

I. INTRODUCTION

A large volume of work has been produced on the wake of submerged bodies travelling horizontally through stably stratified fluids of linear density gradients. The internal Froude number, Fr, characterizes the undisturbed density gradient of the fluid stratification and is defined as the ratio of the submerged body speed to the product of its characteristic vertical length scale and the Brunt-Väisälä frequency of the fluid. The Reynolds number, Re, is the viscous similarity parameter for the submerged body, and it is defined as the ratio of the body speed and length scale to the viscosity of the fluid.

One of the distinctive features of this stratified flow, as opposed to the flow of a uniform density fluid, is that the stratification produces a gravity-induced restorative buoyancy force due to the displacement of particles away from their original hydrostatically balanced equilibrium positions. When the wake is oriented horizontally, this buoyancy force breaks the full axial symmetry of the wake around the submerged body and may directly affect physical flow features ahead, around, and behind the body. Although many experimental configurations for the travelling body can be employed, the sphere is identified as a canonical configuration in the study of far wake characteristics.[1,2]

[a)]Electronic mail: trevoror@usc.edu
[b)]Electronic mail: jad@usc.edu. Tel.: 213-740-5357.
[c)]Electronic mail: geoff@usc.edu. Tel.: 213-740-4132.
[d)]Electronic mail: sconstan@engineering.uiowa.edu. Tel.: 319-384-0630.

The wake of a sphere traveling horizontally through a linearly stratified fluid is categorized into three major regions: the near wake, the non-equilibrium (NEQ) regime,[3] and the far wake, also noted as the quasi-2D (Q2D) regime.[3] Each of these regions has been studied experimentally, analytically, and numerically, but until now, there have been no detailed descriptions of self-contained multiple field components in the near wake of the sphere for any fluid of significant stratification.

The current work is motivated by ongoing computational efforts to model the flow field development of the wake of a linearly stratified fluid flow around a sphere. The first numerical study to include a sphere explicitly within the computational domain for a linearly stratified flow is that of Hanazaki.[4] Hanazaki performed steady, $Re = 200$ simulations across a wide range of $Fr = [0, 200]$ to study the effects of lee waves and stratification on the sphere itself. Recently, two quantitative studies have explicitly accounted for the presence of the sphere inside the computational domain for high Reynolds number simulations. Rottman *et al.*[5] performed simulations for $Fr = \{1, 4\}$ by use of an immersed boundary method. Second, Pasquetti[6] performed "large eddy simulation (LES)-like" simulations at $Re = 10^4$, $Fr = 50$, accounting for the sphere with a "pseudo-penalization" method.

Other recent interest with respect to wake simulation in stratified flows is in the quantitative analysis of wake generated internal waves and the formation of far wake "pancake" eddies. Fung and Chang[7] performed turbulence modelling of the far wake with anisotropic closure schemes and studied the formation of pancake eddies and the free surface response to their presence. Gourlay *et al.*[8] continued the numerical investigations on the formation of the pancake eddies by using direct numerical simulation (DNS). Their $Re = 10^4$, $Fr = 10$ simulations showed that the far wake pancake eddies eventually form without the prior presence of coherent structures. The success of these simulations has encouraged successive simulations of the NEQ and far wake regions. Additional simulations investigating the NEQ and far wake using DNS,[8,9] LES,[10] or multi-domain spectral element penalty methods[11,12] also initialize their stratified wake simulations without explicitly accounting for the sphere.

There is a continued interest in development of numerical stratified wake simulations, and related studies show a trend of considering the computational domain to represent a region that is physically close to the sphere, most commonly associated with the near wake region. The exact initial conditions and initialization procedures have varied: *ad-hoc* representation of the sphere,[7] experimental fits of uniform density wakes,[8–10,13] and extrapolation of post-NEQ experimental data.[11]

Each numerical study that initializes its simulation without explicitly accounting for the sphere utilizes an additional relaxation procedure[8–12] to allow the turbulent velocity field to develop prior to analyzing the subsequent integration of the governing equations. Equipartition of turbulent energy is assumed during the initialization process, and an initial density field is not specifically prescribed. Pasquetti[6] initialized a far wake simulation by interpolating the wake of a sphere explicitly within the domain and found that the time/distance behind the sphere at which the pancake eddies form could change by a factor of 5.[6]

This work is a successor to that of Hanazaki[4] because the sphere is explicitly accounted for in the simulation domain, and the wake features are unsteady. Initially, simulations at Reynolds number of $Re = 5000$ were performed using Detached Eddy Simulations (DESs), and the results are reported elsewhere.[14] However, to limit uncertainties due to turbulence modelling, the simulations reported here are focused at lower $Re = 1000$, without relying on turbulence modelling or immersed boundary treatments, and a self-consistent data field of velocity and density is collected. Despite difference in Reynolds numbers, DNS and DES results are in a qualitative agreement, suggesting that the collected database may be useful even at Re larger than 1000. Capturing the density field within the wake is challenging to obtain experimentally across a wide range of stratified fluids because experimental studies of the wake density have typically used conductivity probes and/or rakes.[15–18] Computational investigations that explicitly contain the sphere are in an advantaged position to generate the entire velocity and density field across a wide, uncoupled (a useful feature[19]) parameter space in an efficient manner.

II. PHYSICAL PROBLEM

The stable, linearly stratified fluid is governed by the incompressible Navier Stokes equations in the Boussinesq approximation.[6–13] The non-dimensional governing equations are

$$\frac{\partial \vec{u}}{\partial t} + \vec{u} \cdot \vec{\nabla}\vec{u} + \vec{\nabla} p - \frac{1}{Re}\nabla^2 \vec{u} + \frac{\rho'}{Fr_D^2}\vec{k} = 0, \tag{1}$$

$$\vec{\nabla} \cdot \vec{u} = 0, \tag{2}$$

$$\frac{\partial \rho'}{\partial t} + \vec{u} \cdot \vec{\nabla}\rho' - w - \frac{1}{Pr\,Re}\nabla^2 \rho' = 0. \tag{3}$$

Non-dimensionalization is achieved by defining

$$t = t^* \frac{U_s^*}{D^*}, \quad \vec{x} = \frac{\vec{x}^*}{D^*}, \quad \vec{u} = \frac{\vec{u}^*}{U_s^*}, \quad p = \frac{p^*}{\rho_o^* U_s^{*2}}, \quad \rho' = \frac{\rho'^*}{\left[-D^* \frac{\partial \rho^*(z)}{\partial z}\right]}. \tag{4}$$

By convention, all quantities denoted by an asterisk are dimensional. Non-dimensional time is t, and U_s^* and D^* are the sphere speed and diameter, respectively. The reference density of the fluid is ρ_o^*. The spatial coordinates are $\vec{x} = (x, y, z)$ and the flow field velocity vector is denoted $\vec{u} = (u, v, w)$ and the perturbation pressure is denoted by p. The density perturbation is normalized by $\partial \rho^*(z)/\partial z$, which is the upstream, undisturbed fluid density gradient and is constant in a linearly stratified fluid. All vectors are defined in the standard Cartesian basis set $\{\hat{i}, \hat{j}, \hat{k}\}$, where $\hat{i}$ is directed opposite to the steady motion of the sphere and $x = 0$ is located at the sphere center. Field quantities (i.e., $\vec{u}$, p, and ρ') vary with space and time.

To obtain Eq. (1), the fluid density is decomposed, and hydrostatic balance is used to equate a background pressure gradient with a background stratification,

$$\rho^*(\vec{x},t) = \rho_0^* + \rho^*(z) + \rho'^*(\vec{x},t), \tag{5}$$

$$P^*(\vec{x},t) = P^*(z,t) + p^*(\vec{x},t), \tag{6}$$

$$\frac{\partial P^*(z,t)}{\partial z} = -g^* \rho_0^* - g^* \rho^*(z), \tag{7}$$

where $P^*(\vec{x},t)$ is the total pressure and $P^*(z,t)$ is a background pressure. The total density field is $\rho^*(\vec{x},t)$, $\rho'^*(z)$ is the undisturbed vertical density distribution, and g^* is the sole component of gravity in the $-\hat{k}$ direction.

The non-dimensional parameters are

$$Re = \frac{U_s^* D^*}{\nu_o^*}, \quad Pr = \frac{\nu_o^*}{\kappa_o^*}, \quad Fr = \frac{U_s^*}{N^* R^*} \equiv 2\frac{U_s^*}{N^* D^*} = 2Fr_D,$$

where Re is the Reynolds number, Pr is the Prandtl number, κ_o^* is a constant reference thermal diffusivity of the fluid, ν_o^* is a constant reference viscosity, ρ_o^* is a constant reference density, and R^* is the sphere radius.

The constant Brunt-Väisälä frequency is denoted by N^*, in units rad s^{-1}, and defined for the Boussinesq fluid by

$$N^{*2} = -D^* \frac{g^*}{\rho_o^*} \frac{\partial \rho^*(z)}{\partial z}. \tag{8}$$

The Prandtl number is a fluid property and represents the ratio of momentum to thermal diffusivity of the fluid. Typically, the Re is an indicator of the range of all dynamic scales present in the fluid flow. If $Pr > 1$, then the range of dynamic scales for the density in Eq. (3) is larger than for the velocity in the Navier-Stokes equations, Eq. (1), at given Re. In numerical simulations, this requires higher spatial resolution than implied by the value of the Reynolds number only. To avoid this difficulty, we are setting Pr formally to unity, with the expectation that the current simulations correctly represent the large scale flows in the near wake region of thermally stratified water at a $Pr = 7$, or even a salt-stratified water at a $Pr \simeq 700$, but are not expected to resolve the finest scale details of the scalar field that are present in such fluids.

The square of the internal Froude number, Fr, may be viewed as a representation of mean kinetic energy to the energy required for a particle to move over the top of the sphere in the $z = 0$ plane, but Fr is representative of other buoyant characteristics of the flow. As reviewed by Hopfinger *et al.*[20] and Bonneton *et al.*,[21] with respect to a reference frame attached to the steadily, horizontally translating sphere, a characteristic, stationary lee wave has a frequency

$$\omega_b^* = U_s^* k^*, \tag{9}$$

where k^* is the horizontal wave number of dimension m^{-1} and ω_b^* is the buoyancy frequency in units rad s^{-1}. The maximum buoyancy frequency of the fluid is $\omega_b^* = N^*$, and if Eq. (9) is non-dimensionalized by defining $k = k^* D^*$,

$$k = \omega_b^* \frac{D^*}{U_s^*} = \frac{N^* D^*}{U_s^*} = 2Fr^{-1}, \tag{10}$$

and Fr is a measure of a characteristic buoyant wavelength in the lee of the sphere. In this steady, linear approximation, a stationary lee wavelength, λ, is defined $\lambda = 2\pi k^{-1} \equiv \pi Fr$.

III. NUMERICAL METHOD

The numerical method solves the discretized form of Eqs. (1)-(3) in generalized curvilinear coordinates on a non-staggered grid using an alternating direction implicit fractional step method[22] within a parallelized framework.[23] The pseudo-transient residuals are based on $\Delta\vec{Q}_{max}$, where $\vec{Q} = (u, v, w, p, \rho')$ represents the primitive variables, and each element of $\Delta\vec{Q}$ is required to be less than or equal to 10^{-4} to obtain the unsteady converged solution within each physical time step. The required iterations to converge vary between each Fr case but are typically $O(100)$ in the $Re = 1000$ cases.

For low Fr cases, sufficient resolution of the Brunt-Väisälä frequency, represented by Fr, may dictate choice of time step, Δt. For the $Re = 200$ case, which is steady in the uniform density fluid, the resolution of unsteady mechanisms related to Fr is virtually guaranteed. For the $Re = 1000$ cases, the Strouhal number, St, of the unsteady motion of the separation point and unsteady vortex shedding into the near wake is expected to be $St \simeq 0.19$ for the uniform density case.[24] Because the $Re = 1000$ simulations are performed for $Fr \geq 1$, the buoyancy frequencies are assumed to be equivalent or less than that of the large scale frequencies of the wake. Choices of time step for the low resolution $Re = \{200, 1000\}$ simulations are shown in Table I.

The grid is generated with orthogonal spherical coordinates θ, ϕ, and r, which correlate to computational coordinates ξ, η, ζ,

$$r = r_{min} + \left(r_{max} - \frac{1}{2}\right)\left(\frac{\tanh k_1 \left(\frac{\zeta - 1}{\zeta_{max} - 1} - 1\right)}{\tanh k_1} + 1\right), \tag{11}$$

$$\theta = \pi \frac{\xi - 1}{\xi_{max} - 1}, \tag{12}$$

$$\phi = 2\pi \frac{\eta - 1}{\eta_{max} - 2}, \tag{13}$$

subsequently,

$$x = r\cos\theta, \quad y = r\,\sin\theta\cos\phi, \quad z = r\sin\theta\sin\phi, \tag{14}$$

TABLE I. Choice of Δt for each Re/Fr pairing.

				$Re = 200$			$Re = 1000$
Fr	0.10	0.15	0.20	0.275	0.35	$[0.40, \infty]$	$[1.0, \infty]$
Δt	0.005	0.005	0.01	0.0125	0.0125	0.025	0.01

where computational coordinates ξ, η, ζ vary from 1 to ξ_{max}, η_{max}, ζ_{max}, respectively, $r = r^*/D^*$, and parameter $k_1 = 3.8$ is chosen to resolve the thinnest laminar boundary layers of interest and, consequently, causes grid refinement closer to the sphere.

Polar singularities located at $\xi = \{1, \xi_{max} - 1\}$ are extrapolated from the interior of the domain.[25–28] The periodic, azimuthal direction has overlapping grid points located at $(\eta = 1, \eta_{max} - 1)$ and $(\eta = 2, \eta_{max})$. At the surface of the sphere, $\zeta = 1$, a no-slip boundary condition for velocity, $\vec{u} = \vec{0}$, is implemented and a zero normal derivative, $\frac{\partial \rho'}{\partial \vec{n}} = 0$, for the scalar ρ'. The sphere surface is at $r_{min} = 0.5$ and domain inflow/outflow boundaries are at $r_{max} = 60$. Inflow boundary conditions are applied at $\zeta = \zeta_{max}$ from $0 \le \theta < 0.55\,\pi$ where $\vec{u} = (1,0,0)$ and $\rho' = 0$. Outflow boundary conditions are applied at $\zeta = \zeta_{max}$ from $0.55\,\pi \le \theta \le \pi$.

A damping layer is present in the simulations due to the potential of numerical boundary reflections of internal waves that are generated by the sphere and its wake. The layer is implemented by adding a forcing term to the governing equations, Eqs. (1) and (3),

$$GE(\vec{Q}) + f(\vec{x})(\vec{Q} - \vec{Q}_{ave}) = 0, \tag{15}$$

where GE is the governing equation for any component of $\vec{Q} = (u, v, w, \rho')$ and $f(\vec{x})$ contains the spatially varying damping coefficient. By choice, $\vec{Q}_{ave} = (U(\vec{x}), 0, 0, 0)$, where $U(\vec{x})$ is the spatially varying, time-averaged stream-wise velocity component. The damping coefficient is zero for $x \le 15, |y| \le 8, |z| \le 8$ and reaches its maximum just before the outer domain limits. The long length of this layer along with the gradually varying damping coefficient, in conjunction with a sufficient placement of nodes within the damping layer, mitigates numerical reflection of waves from the computational boundary and their interaction within the computational region of interest.[29]

Most runs are performed using a grid size of $N_\xi \times N_\eta \times N_\zeta = 120 \times 120 \times 201$ (the standard resolution). The equations of motion, Eqs. (1) and (3), are solved directly without any additional explicit turbulence modelling. Convective terms for the governing equations are discretized using a 2nd order upwind scheme. These simulations span a fairly wide parameter space of Fr for $Re = \{200, 1000\}$.

Two additional simulations at $Re = 1000$ and $Fd = \{4, \infty\}$ are performed with a higher resolution of $N_\xi \times N_\eta \times N_\zeta = 180 \times 180 \times 501$ grid points using 5th-order upwind scheme and an hyperbolic stretching function for the polar grid point distribution similar to the radial one in Eq. (11), similar to Mittal.[30] The radial stretching parameter in these two cases is modified to $k_1 = 3.3$, and the polar stretching parameter is 1.5. This distribution concentrates two-thirds of the grid points behind the sphere, increases the uniformity of the grid point distribution along the wake centerline, and increases the grid resolution over the standard resolution cases by about a factor of 10.

There are several potential sources of uncertainties in the current simulations such as a presence of damping layers to control reflection of waves from the computational boundary and a residual numerical dissipation associated with upwind schemes employed. The numerical dissipation sometimes may play a role similar to the role of subgrid-scale models in LESs, resulting in the so-called implicit LES (ILES) or no-model LES. Such methods can accurately capture the larger scales of a flow but cannot accurately predict small scales on the order of a grid size. Quantifying these effects is difficult, e.g., the numerical dissipation depends on the mesh size, time step, and the flow itself. To gain confidence in the simulation results, we use traditional, indirect validation procedures by running some cases on different meshes, described above, and comparing our results with experimental results and other numerical simulations.

IV. RESULTS

A. Uniform density fluid

The wake of a sphere travelling steadily through a uniform density fluid at $Re = 200$ is commonly studied.[25,31,32] The wake is considered steady and generates an axisymmetric recirculation region attached to the lee of the sphere. The lower resolution simulations indicate that the non-dimensional length of this laminar recirculation region, measured from the center of the

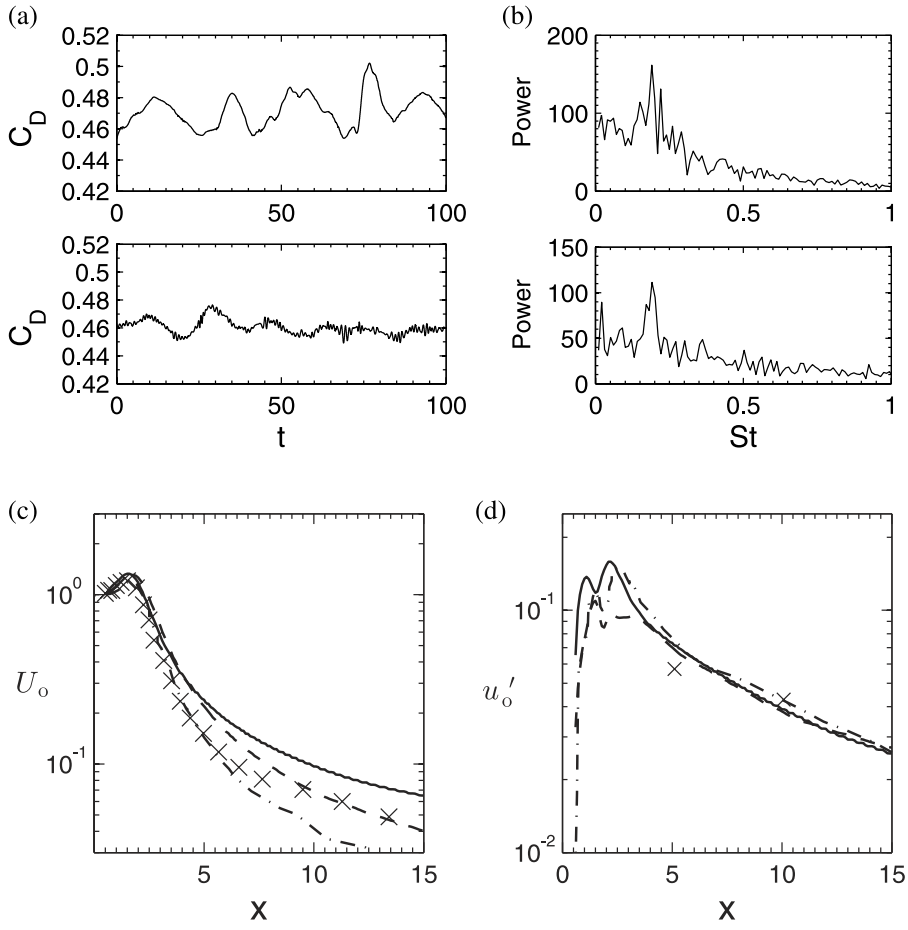

FIG. 1. Re = 1000, Fr = ∞. (a) Sampled stream-wise drag coefficient. Top—low resolution, bottom—high resolution. (b) Power spectra of time history of u at $x \simeq 5$. Top—low resolution, bottom—high resolution. (c) U_o is the centerline, mean stream-wise defect velocity. (d) u'_o is the centerline rms stream-wise perturbation velocity. (−) low resolution, (−−) high resolution, (− · −) Tomboulides and Orszag,[24] (X) Wu and Faeth[33] at Re = 930.

sphere, is $L_b = 1.95$. The stream-wise drag coefficient is $C_{Dx} = 0.757$. Both of these quantities are consistent with prior findings.[25,31,32]

At $Re = 1000$, the uniform density flow is unsteady and very close to the near-transition region.[34] Samples of C_{Dx} produced by the low and high resolution simulations are shown in Figure 1(a). The two curves are aligned for comparative purposes. The differences are in peak magnitudes and the higher frequency oscillations between the two cases. Overall, these two curves show similar quantitative and qualitative behavior. The time-averaged stream-wise drag coefficient in the standard resolution simulation is $\overline{C_{Dx}} = 0.466$ and the high resolution simulation produces a $\overline{C_{Dx}} = 0.460$, which is comparable to experimentally reported values.[35]

Four probes are placed in the wake at $x = 5.75$ and in the vertical and horizontal planes about the wake centerline at a distance of $r_p = 0.6$ in the high resolution simulations and $x \simeq 5, r_p \simeq 0.675$ in the low resolution ones. The power spectrum of $u(\vec{x},t)$ is averaged between the probes and produces the spectrum shown in Figure 1(b). The strongest frequency for both resolutions is at $St = 0.191$. This is the Strouhal number associated with the primary vortex shedding and the overall structure of the wake. Both simulations capture a shear instability frequency[34,36] at $St = 0.36$, shown in Figure 1(b). The high resolution case peak is more prominent, perhaps due to the position of the probe placements.

Values of the mean stream-wise centerline velocity defect, U_o, and root-mean-square (rms) stream-wise velocity perturbation component are shown in Figures 1(c) and 1(d). There is a fairly

good agreement among all plotted cases for the rms stream-wise velocity. Similarly, the unsteady recirculation region length based on the inflection of U_o about 1 is measured to be $L_{rr} \simeq 2.25$, which agrees with prior investigations.[24,37] The curves for U_o in the high resolution and standard resolution simulations overlap up to $x \approx 5$ and diverge at larger x with the difference at the maximum $x = 15$ about 0.02, which is on the order of $1\% - 2\%$ of the peak value of U_o in the domain. There is also similar measure of error in Fig. 1(c) between the spectral results and the high and standard resolution simulations along the centerline, with the spectral results below our data. These differences may be due to the fact that spectral methods have negligible numerical dissipation while most other common methods, such as finite difference and finite volume, are often burdened by unknown numerical dissipation because of the truncation errors of a numerical scheme that diminishes with increasing resolution much slower than for spectral methods.[38] In Fig. 1(c), values of U_o at $x = 15$ decrease for decreasing (presumed) numerical dissipation, similar to the observed trend in experiments of Wu and Faeth[33] where results for $Re = 930$ lie below results for $Re = 300$, i.e., results for the case with less physical, viscous dissipation, are below data for the case with higher physical dissipation. Further discussion of the near wake characteristics is deferred until Secs. IV D, IV F, and IV G.

B. Re = 200, linearly stratified fluid

A natural starting point is to compare simulation results with Hanazaki[4] at $Re = 200$. The flow field is steady, except in the case of very stratified flows which should exhibit unsteady vortex shedding.[39] Results obtained for time-averaged $\overline{\Delta C_{Dx}}$ as a function of Fr are presented in Figure 2(a) where

$$\Delta C_{Dx} = C_{Dx}(Re, Fr) - C_{Dx}(Re, \infty), \tag{16}$$

where $C_{Dx}(Re, \infty)$ is the stream-wise drag coefficient of the sphere in a uniform density fluid at a particular Re. The overbar of $\overline{\Delta C_{Dx}}$ denotes a time-averaging for the unsteady cases. By Eq. (16), $\overline{\Delta C_{Dx}}$ represents the change in drag coefficient of the sphere due to the stratification of the fluid. The simulation agrees with prior investigation[4,5,40] values of $\overline{\Delta C_{Dx}}$ for $Fr \gtrsim 0.5$. When $Fr \lesssim 0.5$, the current simulations disagree completely with Hanazaki,[4] corroborate those of Rottman *et al.*,[5] and generally reproduce the results of Lofquist and Purtell[40] until $Fr < 0.2$.

When $Fr < 0.5$, the flow has a horizontal orientation, and vertically oriented, coherent vortices are shed, as seen in Figure 3(a), whereas when $Fr \geq 0.5$ in Figure 3(b), there is no vortex shedding. At $Fr = 0.2$, the simulations produce a $St_y = 0.19$ at $Re = 200$. Chomaz *et al.*[39] also noted a

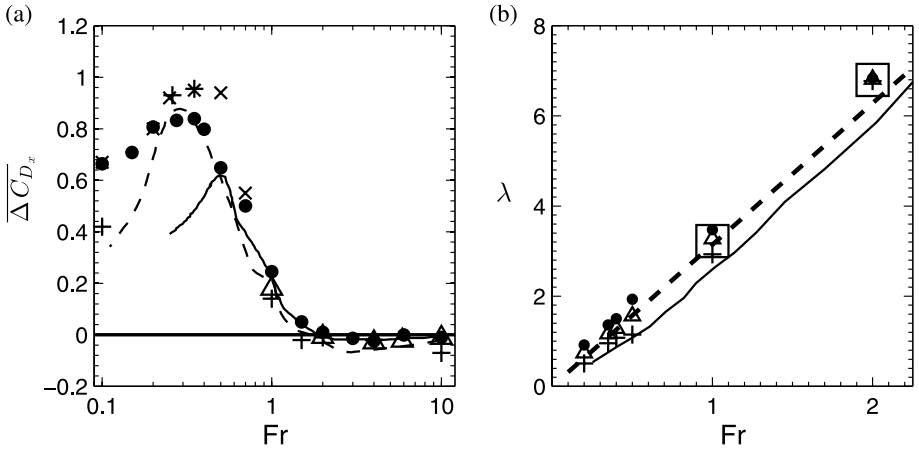

FIG. 2. (a) Change in stream-wise drag coefficient due to stratification. (−) Hanazaki,[4] (−−) Lofquist and Purtell,[40] {× (low-res), + (med-res)} Rottman *et al.*,[5] low resolution simulations at (•) Re = 200, △ Re = 1000. (b) Calculated λ: (−) Hanazaki,[4] (−−) linear theory, low resolution simulations {+, △, •} at $z = \{0.5, 1.0, 1.5\}$ for Re = 200, □ at $z = 1.0$ for Re = 1000.

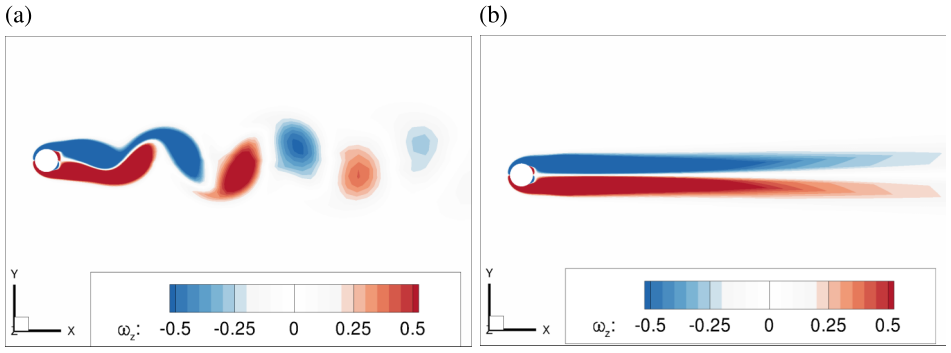

FIG. 3. Re = 200. Instantaneous vertical vorticity, ω_z, on plane defined by $z = 0$: (a) $Fr = 0.4$, (b) $Fr = 0.5$.

general Strouhal number of approximately 0.2 at $Re = 2000$ and $Fr = 0.3$. In this regime, there are small-amplitude oscillations of the stream-wise drag coefficient where $St_x \simeq 2\,St_y = 0.37$, as shown by Figure 4. Simulation results are in agreement with experimental values[40] of $\overline{\Delta C_{Dx}}$ until $Fr < 0.2$.

When $Fr < 0.2$, the current simulations likely have an insufficient resolution for this severely stratified fluid. The current simulations and the low-resolution simulations[5] at $Fr = 0.1$ concur with a value of $\overline{\Delta C_{Dx}} \simeq 0.80$. Between the low- and mid-resolution cases[5] at $Fr = 0.1$, the discrepancies in $\overline{\Delta C_{Dx}}$ and experiment[40] tend to disappear, indicating that increased resolution in future simulations would allow further investigation into these very low Fr flows if they were of interest.

It may be suggested[4,41,42] that a Re effect accounts for the discrepancy between experimental data[40] and the computations of Hanazaki.[4] For $Re = 200$, current results remain consistent with experiments until low Fr values. Review of the experimental data[40] indicates that for $Fr \lesssim 0.25$, the highest Re case is $Re \simeq 550$, and the lowest Re case is $Re \simeq 175$ at $Fr = 0.125$. Flow at these Re is not considered turbulent for uniform density fluids. Turbulent fluctuations in the wake typically occur around $Re = 1000$,[34] and a Re dependence does not sufficiently explain the discrepancies between the $\overline{\Delta C_{Dx}}$ curves.

The current simulations show (see Figure 2(b)) comparable λ values to both Hanazaki[4] and linear theory. Measurements of λ are calculated by the distance between inflections of $\overline{w(\vec{x},t)} = W(\vec{x}) = 0$ (i.e., Figure 5) at different vertical heights on the plane $y = 0$ at $z = \{0.5, 1.0, 1.5\}$. The overbar indicates time-averaging for the unsteady flow cases. Considering the differences between $\overline{\Delta C_{Dx}}$ evident in Figure 2(a) and the agreement on λ in Figure 2(b), sufficient resolution of the lee waves is also not a cause for discrepancy with Hanazaki[4] when $Fr < 0.5$.

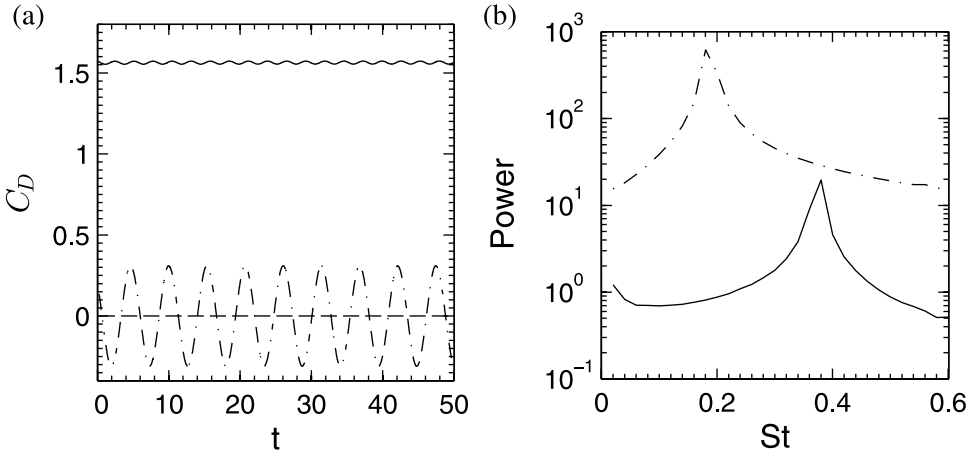

FIG. 4. Re = 200, Fr = 0.4. (−) C_{Dx}, (− · −) C_{Dy}, (−−) C_{Dz}. (a) Components of drag coefficient. (b) Power spectra (C_{Dz} omitted).

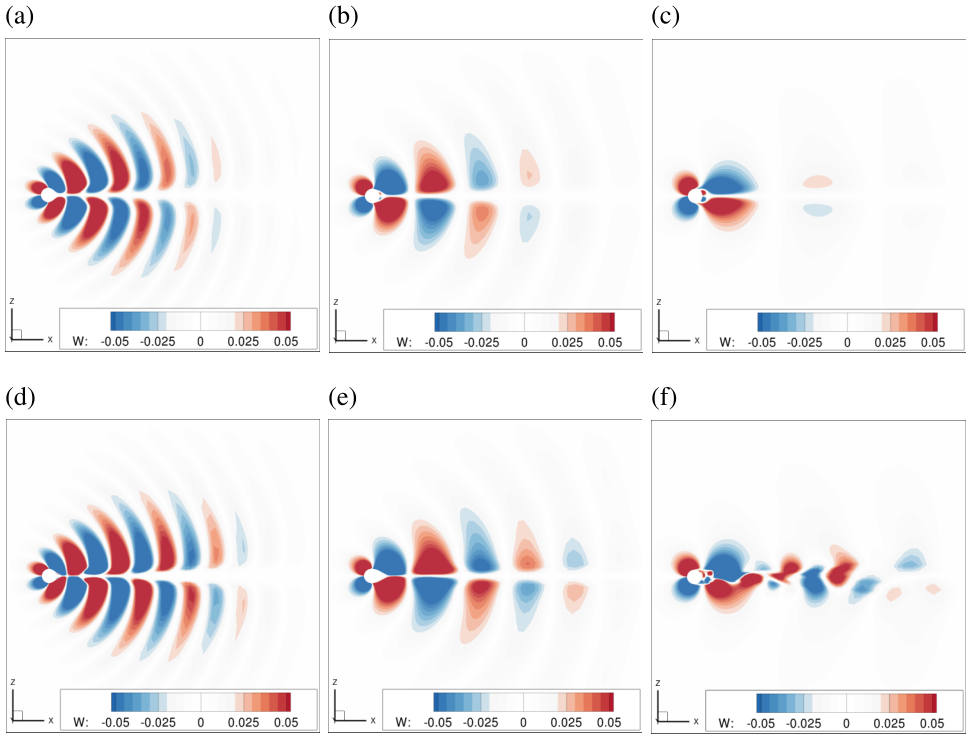

FIG. 5. Contours of instantaneous vertical velocity, w, on plane at $y = 0$. The sphere is centered at $x = y = z = 0$. Re = 200: (a) $Fr = 1$, (b) $Fr = 2$, (c) $Fr = 4$. Re = 1000: (d) $Fr = 1$, (e) $Fr = 2$, (f) $Fr = 4$.

By Figure 2(b), there is no significant departure of calculated lee wavelength from linear theory due to the vortex shedding. Brighton[43] postulated that there is a lack of direct interaction between lee waves and vortex shedding, and this is partly confirmed as the Hanazaki[4] low-resolution $(32 \times 32 \times 62)$ simulations are able to reproduce the expected λ values in Figure 2(a) but not the experimental $\overline{\Delta C_{Dx}}$ seen in Figure 2(b).

In the range of highly stratified, $Fr \simeq 0.2$, to uniform density fluids, $Fr = \infty$, the current simulations accurately reproduce the characteristics of a stratified fluid. Results for $Re = 1000$ are focused on $Fr \geq 1$. Severely stratified cases, $Fr < 0.2$, require higher numerical resolution and are not of current interest. All further discussions revolve around the $Re = 1000$ flow, unless otherwise specified.

C. Downstream distance from the sphere in x and Nt

For linearly stratified fluids, the relationship between a commonly used non-dimensional time, $Nt \equiv N^* t^*$, and downstream distance, $x \equiv x^*/D^*$, is given by

$$Nt = x\,(Fr/2)^{-1}, \tag{17}$$

where origins for x and t are located at the sphere center. Analysis of the wake in Nt is a relative distance behind the sphere in terms of the fraction of the Fr-associated characteristic buoyant wavelength and portion of completed buoyant period.

Consequently, comparisons between the flow of a uniform density fluid and stratified fluid cannot be properly expressed in terms of Nt since the wake of the uniform density fluid (i.e., $N^* \equiv 0$) cannot have an analytic description in Nt. Intuition suggests that description of the flow in the near wake should asymptote with increasing Fr to the behavior of a uniform density fluid. Thus, x is the preferable choice for descriptions of the wake because the simulations explicitly contain the sphere, and physically relevant descriptions in the limit of $Fr \to \infty$ can be made. Notwithstanding, Nt remains useful in illustrating buoyant commonalities between the stratified unsteady wakes. Both

x and Nt are used throughout remaining discussions, and care is taken to ensure that descriptions in x and Nt correlate to the same physical location behind the sphere. For convenience, the equivalent distance and time behind the sphere are commonly given as a set $\{x,Nt\}$.

D. Averaging in the near wake

Experimental studies of stratified wakes frequently use a digital particle image velocimetry (DPIV) setup[44,45] where a realization of the flowfield within a viewing window is spatially integrated,

$$\langle q\rangle_{x_{wc}}(y,z,t) = \frac{1}{\Delta L}\int_{x_{wc}-\frac{\Delta L}{2}}^{x_{wc}+\frac{\Delta L}{2}} q(\vec{x},t)\,dx, \tag{18}$$

where q is any flow field quantity, x_{wc} is the mid-window downstream position, and ΔL is the streamwise width of the window.

A temporal average over the course of several vortex shedding cycles will eliminate variance of collected wake statistics from the simulation data, i.e.,

$$\overline{q}(x,y,z) = \frac{1}{\Delta T}\int_{t_0}^{t_1} q(\vec{x},t)\,dt, \tag{19}$$

where ΔT is the representative time scale of averaging. The period used for computing $\overline{q}(x,y,z)$ is longer than that which is involved in the assumption that a spatial and time average are equivalent.[10]

To highlight the differences between $\overline{q}(x,y,z)$ and $\langle q\rangle_{x_{wc}}(y,z,t)$, and the variance of $\langle q\rangle_{x_{wc}}(y,z,t)$, a computationally generated unsteady flow field is analyzed using a DPIV setup[44,45] for a $Re = 1000$, $Fr = 4$ flow. Figure 6(a) serves as a physical reference to the planes referred to in the DPIV arrangement, and Figure 7(a) serves as an illustrative reference to the DPIV setup and its subsequent effect on statistical data when applied within the near wake.

The visualization/analysis window in Figure 7(a) is centered at $\{x,Nt\} = \{6,3\}$ and $z = 0$, of width $\Delta X = 3.5$, and is coplanar with the $y = 0$ vertical center plane. The visualization plane is integrated spatially to obtain an averaged stream-wise velocity profile,[44]

$$U_{x_{wc}}(0,z,t) = \langle u(\vec{x},t)\rangle_{x_{wc}} = \frac{1}{\Delta X}\int_{x_{wc}-\frac{\Delta X}{2}}^{x_{wc}+\frac{\Delta X}{2}} u(\vec{x},t)\,dx. \tag{20}$$

This average velocity is then assumed to be the average stream-wise velocity everywhere within the visualization window. The root mean square perturbation values are then calculated spatially along

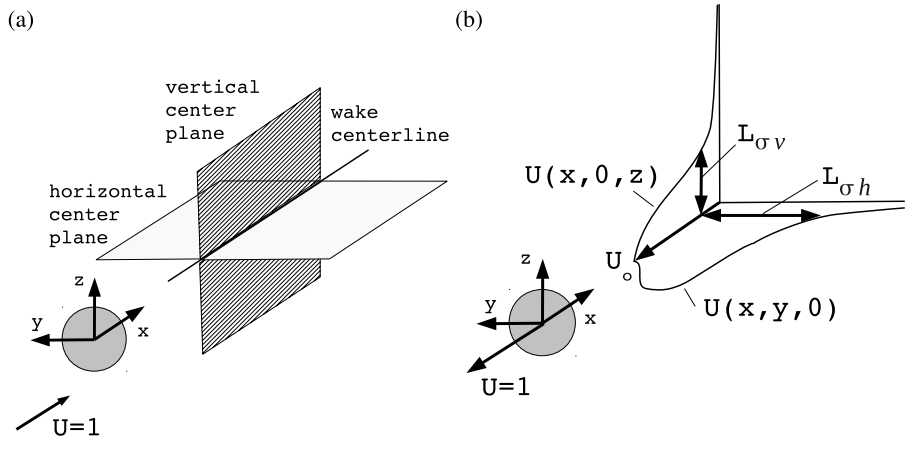

FIG. 6. Sketches (not to scale). (a) Vertical and horizontal center planes and wake centerline. (b) Galilean transformation of stream-wise velocity profiles in upper vertical plane and negative horizontal plane and wake length scales $L_{\sigma v}$ and $L_{\sigma h}$.

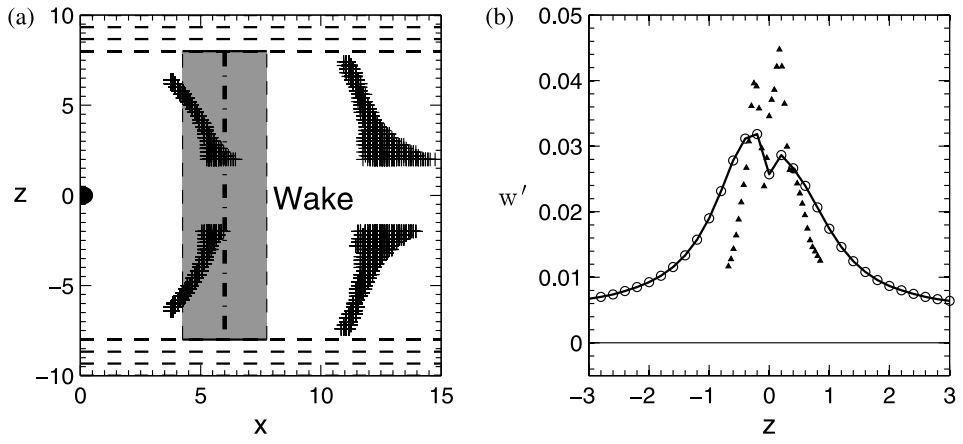

FIG. 7. $Re = 1000$, $Fr = 4$. (a) Shaded area is a DPIV window centered about $x_{wc} = 6$. The sphere at $(x, z) = (0, 0)$ is moving to the left. (−−) damping layer. (+) detected locations for $|z| > 2$ and $3.75 \le x \le 14.75$ where $w'(x, 0, z, t) \lesssim 10^{-3} \simeq 0$ over a $\Delta T = 40$; sampled every 0.4 time units. (b) (− · −) simulation comparison of $\overline{\langle w' \rangle}_{x_{wc}}(0, z)$ to (▲) Spedding[44] at $Re = 5000$.

the stream-wise direction,[44]

$$\langle u' \rangle_{x_{wc}}(0,z,t) = \left[\frac{1}{\Delta X} \int_{x_{wc}-\frac{\Delta X}{2}}^{x_{wc}+\frac{\Delta X}{2}} \left[u(x,0,z,t) - U_{x_{wc}}(0,z,t) \right]^2 dx \right]^{\frac{1}{2}}, \tag{21}$$

$$\langle v' \rangle_{x_{wc}}(0,z,t) = \left[\frac{1}{\Delta X} \int_{x_{wc}-\frac{\Delta X}{2}}^{x_{wc}+\frac{\Delta X}{2}} v(x,0,z,t)^2 dx \right]^{\frac{1}{2}}, \tag{22}$$

$$\langle w' \rangle_{x_{wc}}(0,z,t) = \left[\frac{1}{\Delta X} \int_{x_{wc}-\frac{\Delta X}{2}}^{x_{wc}+\frac{\Delta X}{2}} w(x,0,z,t)^2 dx \right]^{\frac{1}{2}}, \tag{23}$$

where $x_{wc} = 6$ is the x location about which the example analysis window (shaded area of Figure 7(a)) is centered in the stream-wise direction.

Comparisons of the low resolution simulation are made against experimentally collected DPIV field data taken in the near wake at $Re = 5000$, $Fr = 4$ (Fig. 8 of Spedding;[44] reproduced in Figure 7(b)). In the stratified near wake, this is possibly the only in-plane stream-wise and vertical perturbation velocity data set available. Although the current simulation is performed at $Re = 1000$, the uniform density case is a highly unsteady, near-transition flow, and comparisons between the statistically collected data sets remain of interest as wake behavior between $Re = 1000$ and $Re = 5000$ is expected to be similar.

At $Fr = 4$, the computationally obtained quantities in Eqs. (21)-(23) are spatially averaged as indicated and an additional average in time is applied to a series of windows of the same dimension centered about $\{x, Nt\} = \{6, 3\}$ such that at $y = 0$,

$$\overline{\langle q \rangle}_{x_{wc}}(0,z) = \frac{1}{\Delta T} \int_{t_0}^{t_1} \langle q \rangle_{x_{wc}}(0,z,t) dt. \tag{24}$$

The interval of the time average is $\Delta T = 40$ and is intended to remove any variance in the collected statistics at that location. If time and spatial averaging are equivalent, or roughly equivalent, then there should be no significant penalty in comparison from the double averaging technique.

Equation (23) assumes that $W(x_{wc}, 0, z, t) = 0$, and all fluctuating quantities in the vertical direction contribute to $\langle w' \rangle_{x_{wc}}(0, z, t)$ only. The computational results for $\overline{\langle w' \rangle}_{x_{wc}}(0, z)$ are compared against the $Re = 5000$, $Fr = 4$ experimental data in Figure 7(b). In the double-averaging technique, regions of non-negligible vertical perturbation velocities appear in Figure 7(b), and $\overline{\langle w' \rangle}_{x_{wc}}(0, z)$ extends out of the wake region for $|z| \ge 2$, where the value of $|z| = 2$ is the current choice in demarcating the wake and free stream regions. In that same figure, the computed profile

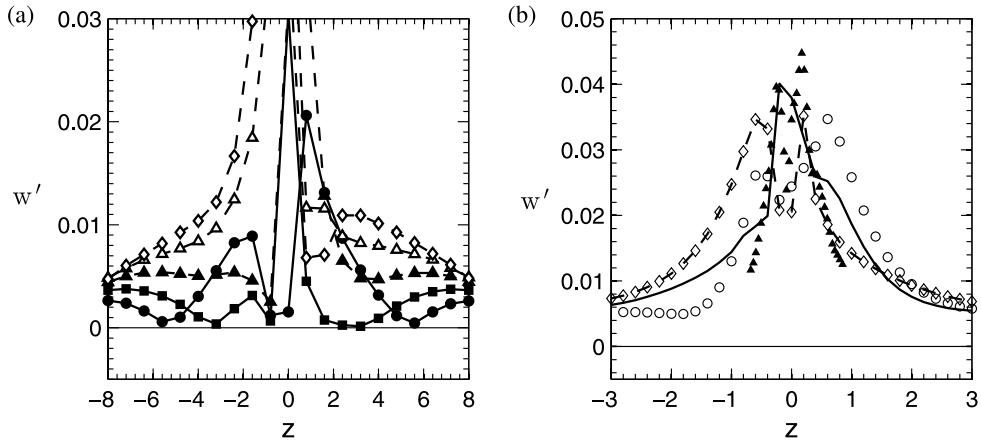

FIG. 8. $Re = 1000$, $Fr = 4$. (a) $w'(\vec{x}, t = 20)$ in vertical plane for $(-\bullet-)$ $x = 4.45$, $(-\blacksquare-)$ $x = 5.25$, $(--$ w/▲$)$ $x = 6.05$, $(--$ w/△$)$ $x = 6.85$, $(--$ w/◇$)$ $x = 7.65$. (b) $\langle w' \rangle_{x_{wc}}(0, z, t)$ in vertical plane at $(\circ)$ $t = 0$, $(-)$ $t = 20$, and $(-\cdot-$ w/◇$)$ $t = 40$ at $x_{wc} = 6$; ▲ Spedding[44] at $Re = 5000$.

of $\overline{\langle w' \rangle}_{x_{wc}}(0, z)$ is also wider in z than the experimentally collected $\langle w' \rangle_{x_{wc}}(0, z, t)$. This collective difference is referred to as the "tails" of the perturbation quantity data. They could suggest evidence of internal waves being generated outward from the unsteady wake motion, wave reflections from the finite numerical boundary, or some combination thereof. However, the origin of both the non-negligible regions of $\overline{\langle w' \rangle}_{x_{wc}}(0, z)$ in Figure 7(b) for $|z| \geq 2$ and the width of the $\overline{\langle w' \rangle}_{x_{wc}}(0, z)$ curve for $|z| < 2$ is results of the averaging techniques being applied in the near wake.

If $W(x_{wc}, 0, z, t) \equiv 0$, the z location where $w'(x, 0, z, t) \simeq 0$ (locations of lee wave crests and troughs as per linear theory[46]) will certainly change in x. This behavior is qualitatively shown in Figure 7(a), and the lines of constant phase for lee waves are curved but not necessarily in accordance with linear theory.[39] Using a temporally sampled subset of the data used to create Figure 7(a), the results in Figure 8(a) for values of $w'(x, 0, z, t)$ show that there are indeed x locations where $w'(x, 0, z, t) \simeq 0$ at a specific z location, occurring within Figure 8(a) at $(z, x) = (\pm 5.6, 4.45)$ and $(z, x) = (\pm 3.2, 5.25)$. In Figure 7(a), there are subsequent downstream locations between the lee wave crests and troughs in x where $w'(x, 0, z, t) \not\simeq 0$ anywhere in the far field between $6.05 \leq x \leq 7.65$, denoted by the double dashed lines. These trends correlate with Figure 7(a) where between $8 \lesssim x \lesssim 12$ no $w'(x, 0, z, t) \simeq 0$ is detected.

Because the width of the wake profile for $\overline{\langle w' \rangle}_{x_{wc}}(0, z)$ is also wider than the experimental results presented in Figure 7(b), the variation of the width of $\langle w' \rangle_{x_{wc}}(0, z, t)$ in time is also addressed. Three spatially averaged windows for $\langle w' \rangle_{x_{wc}}(0, z, t)$ at arbitrary times $t = \{0, 20, 40\}$ are compared against the experimental data in Figure 8(b). From the three discrete-time profiles, it is apparent that the $\langle w' \rangle_{x_{wc}}(0, z, t)$ profile significantly varies in time, and at some times (e.g., $t = 20$), the computational results produce a profile width for $\langle w' \rangle_{x_{wc}}(0, z, t)$ comparable to the experimental results. The fluctuations in the width of the profile for $\langle w' \rangle_{x_{wc}}(0, z, t)$ are related to the overall unsteadiness of the near wake structure itself.

If the DPIV window is spatially integrated and $W(x_{wc}, 0, z, t) = 0$, the majority of x locations contribute some non-zero quantity to $\langle w' \rangle_{x_{wc}}(0, z, t)$ in the free-stream region, thereby creating the tails' non-zero asymptote with increasing $|z|$ as seen in Figure 7(b). The free-stream values for $\langle w' \rangle_{x_{wc}}(0, z, t)$ will be dependent on the width and the location of the DPIV averaging window and the time of the spatial integration. A similar argument can be made for profiles of v' in the NEQ regime (e.g., Fig. 9 of Spedding[44] at $Nt = 9$). When the assumption $V(\vec{x}, t) = W(\vec{x}, t) = 0$ is removed, which is the case for all data presented after this section, the asymptotic free-stream values of $v'(\vec{x}, t)$ and $w'(\vec{x}, t)$ will approach zero by the onset of the damping layer.

The computational results are presented using only temporal averaging. An inferred benefit of the analysis of the free stream perturbation quantities is that when $w(\vec{x}, t)$ is only averaged in time then there will be an expected free stream z location where $W(\vec{x}) \simeq 0$ for downstream locations of x

that coincide with the crest or trough of a lee wave, and this feature can be utilized (i.e., Figure 2(b), Figure 5, Sec. IV F) when identifying the crests or troughs of lee waves at the edge of the unsteady wake.

The flow field is described using a Reynolds decomposition

$$q(\vec{x},t) = Q(\vec{x}) + q'(\vec{x},t), \tag{25}$$

where $q = (u,v,w,\rho')$ represents the full-field of the primitive variables, $Q = (U,V,W,\overline{\rho'})$ is their time averaged value, and $q' = (u',v',w',\rho')$ are the perturbation quantities. Note that $\rho'(\vec{x},t)$ of Eqs. (3) and (5) is now comprised of an average and perturbation component.

The root mean square of a perturbation component is then defined

$$q'(\vec{x}) = \left[\frac{1}{\Delta T}\int_{t_o}^{t_1}[q(\vec{x},t) - Q(\vec{x})]^2 dt\right]^{1/2}, \tag{26}$$

where $\Delta T = 200$ for the low resolution $Re = 1000$ cases. t_o begins from a statistically steady state based on the time history of the stream-wise drag coefficient, and $t_1 = t_0 + \Delta T$. For brevity, the root mean square perturbation components calculated by Eq. (26) are denoted by the prime only. Although the simulations are performed by considering the inertial frame as attached to the sphere, the flow field is presented in the laboratory reference frame. This is accomplished by Galilean transformation in the streamwise direction because the sphere travels in a steady, horizontal motion. A sketch of the transformation is in Figure 6(b).

E. Numerical resolution at Re = 1000, Fr = 4

In Sec. IV A, it is shown that the high resolution and standard resolution simulations exhibit similar characteristics at $Re = 1000$ and $Fr = \infty$. That case represents the upper limit of the stratified regime of interest. Above $Fr = 4$, the near wake behavior maintains its highly unsteady structure, and a $Fr = 4$ represents the lowest limit of this flow regime of interest. Understanding the effects of the difference in numerical resolution on the range $Fr = [4,\infty]$ and how the statistical trends are affected by this difference are addressed in this section.

In these stratified flow simulations, it is challenging to quantitatively separate the internal waves at the edge of the wake from the wake structure itself using the λ_2-criterion as vorticity is generated by both internal waves and vortical wake structure. Regardless, the isosurfaces of the λ_2-criterion[47] in Figure 9(a) in the low resolution simulations are able to capture the largest scale structures present in the stratified near wake. In qualitative comparison with Figure 9(a), the higher resolution simulation in Figure 9(b) captures more details of the instantaneous near wake structure.

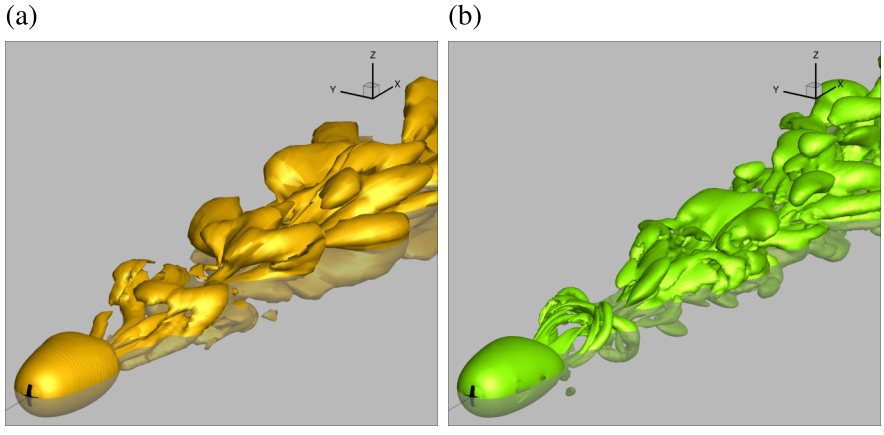

FIG. 9. Re = 1000, Fr = 4. Instantaneous isosurface of λ_2-criterion, defined by $\lambda_2 = -0.001$. (a) Low resolution, (b) high resolution. The grey region is the $z = 0$ plane.

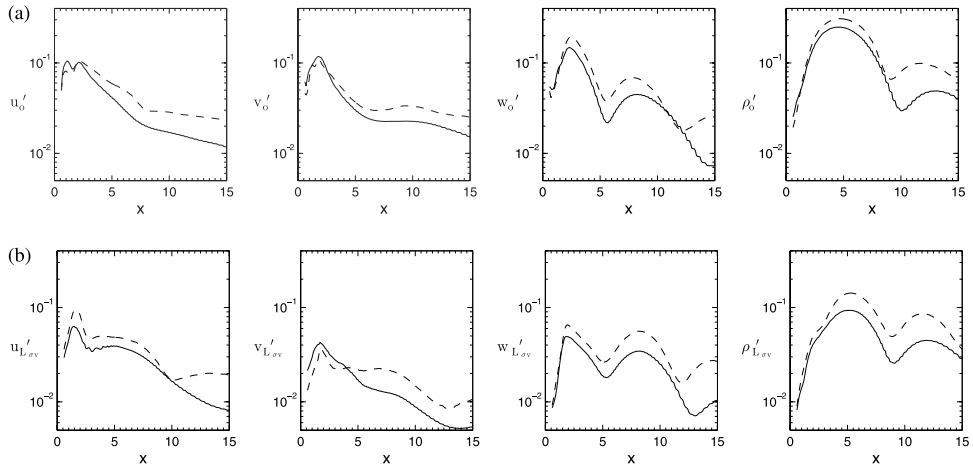

FIG. 10. Re = 1000, Fr = 4. Perturbation quantity comparison (a) on centerline, (b) at $z = L_{\sigma v}$. (−) standard resolution, (−−) high resolution.

Comparison of the resultant centerline perturbation quantities between the low and high resolution simulations is shown in Figure 10(a), and the perturbation quantities at the vertical edge of the wake (defined by $L_{\sigma v}$) are presented in Figure 10(b). The perturbation quantities are consistently larger in the high resolution simulation when compared against the low resolution simulation. The perturbations in u' are larger in the high resolution simulation, but there is also an increased velocity defect in U_o seen in Figure 11 over the low resolution values. The magnitudes for quantities v', w', and ρ' also trend similarly in the near wake. It is of note that the peak magnitude of w'_o at w' at $L_{\sigma v}$ for $x = 6$ in the high resolution simulations is similar to the experimental values obtained by Spedding[44] in Figure 7(b) at their respective locations. Significant departures in qualitative behavior between different resolution simulations occur around or after the near wake value of $Nt \simeq 2 - 3$, where the grid resolution for the standard simulation starts to coarsen away from the near wake region.

Later sections will also focus on a data collapse description of the near wake as a function of Fr and $L_{\sigma v}$. As such, a comparison between the length scales calculated between the high resolution simulation and standard resolution simulation is provided in Figure 12. Critically, the vertical length scales are nearly identical between the high and standard resolution case until a

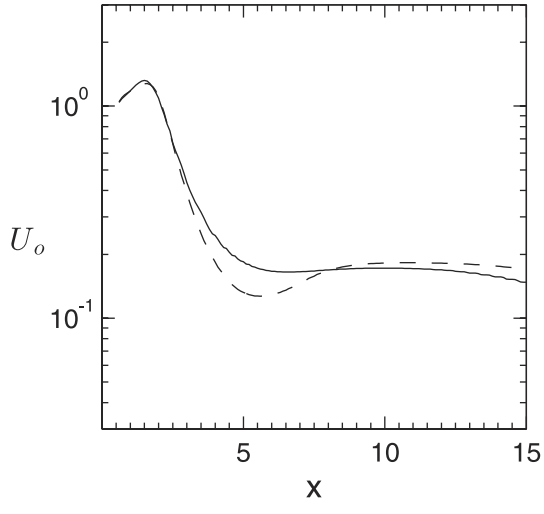

FIG. 11. Re = 1000, Fr = 4. Centerline velocity defect. (−) standard resolution, (−−) high resolution.

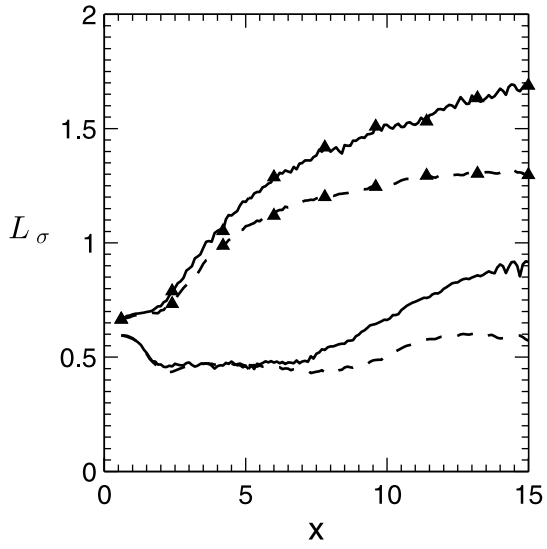

FIG. 12. Re = 1000, Fr = 4. Computed half-widths of the near wake at (−) low resolution and (−−) high resolution. No symbol is vertical length scale, (▲) is horizontal length scale.

downstream position of $x \simeq 8$ or $Nt \simeq 2-3$. This range fully encompasses the region considered to be the near wake of the sphere. Thus, the low resolution simulations are expected to have sufficient resolution to capture the relevant near wake physics for a range of stratified fluids between $Fr = 4$ and $Fr = \infty$ based on the parity of calculated vertical length scales and the agreement of quantitative and qualitative behavior both at the wake centerline and its edges. The low resolution simulations are used in the remainder of the discussion of the near wake behavior.

F. Length scales of the near wake

The horizontal and vertical half-widths of the wake are the definitional choice of wake length scales. The average stream-wise velocity component along the centerline $U(x,0,0) = U_o(x) = U_o$, called the defect velocity, is used to define these length scales. The edges of the wake are defined by locations where $U(\vec{x}) = 0.15\,U_o$ as sketched in Figure 6(b). The horizontal half-width of the wake is denoted by $L_{\sigma h} \equiv L^*_{\sigma h}/D^*$, and the vertical half-height is denoted as $L_{\sigma v} \equiv L^*_{\sigma v}/D^*$. Physical locations where $|y| < L_{\sigma h}$ and $|z| < L_{\sigma v}$ are referred to as inside the wake region, and outside of these bounds is referred to as the free stream, which may or may not contain lee waves of significant amplitude.

When $Fr < 4$, the simulations indicate that the stratification significantly suppresses unsteady motion, consistent with experimental observations[39] at $Re = 2000$. At $Fr = 2$, the flow is essentially steady, and when $Fr = 1$, the flow is certainly steady, with stratification having completely suppressed the statistical fluctuations in the flow. Significant lee waves are also present in the free stream for $Fr < 4$ as can be inferred from results shown in Figures 5(d) and 5(e).

The lee waves have a pronounced effect on the length scale behavior of the near wake for the $Fr = \{1,2\}$ cases as indicated by Figure 13. Initial values of $L_{\sigma v}$ are significantly reduced for $Fr = \{1,2\}$ when compared with the $Fr = 4$ case. After an initial reduction of $L_{\sigma v}$ for both $Fr = \{1,2\}$, the vertical length scale continues to increase in some average sense with x. The vertical flow over the sphere in the $Fr = 1$ case is likely suppressed due to energy restrictions, but $L_{\sigma v}$ between the two cases scales similarly as downstream location increases in x. The oscillations in $L_{\sigma h}$ for the $Fr = 1$ case (Figure 13) do not match the $Fr = 2$ case when $x \gtrsim 1.5$ even though the widths begin at similar values. This is attributed to the significance of the lee wave influence, and inspection of Figure 13 shows local maxima and minima for $Fr = 1$ length scales that are out of phase directly behind the sphere.

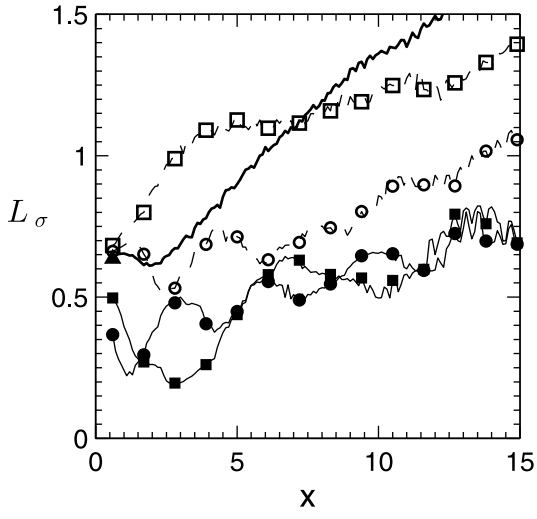

FIG. 13. Re = 1000. Half-widths of the near wake. Open symbols correlate to $L_{\sigma h}$, closed symbols to $L_{\sigma v}$. (○, ●) Fr = 1, (□, ■) Fr = 2, (▲) Fr = 4 for comparison at $x = 0.6$, (–) $Fr = \infty$.

The oscillatory behavior of $L_{\sigma v}$ is correlated with the influence of the average perturbation density, $\overline{\rho'}$. From Eq. (1), $4\,\overline{\rho'}/Fr^2$ is representative of the average vertical body force on the fluid. The correlation between $4\,\overline{\rho'}/Fr^2$ and $L_{\sigma v}$ is shown through Figures 14(a) and 14(b), with data collected at positive $z = L_{\sigma v}$, the vertical edge of the wake, where minima and maxima are in phase with the minima and maxima of $L_{\sigma v}$ in the near wake. As $4\,\overline{\rho'}/Fr^2$ decreases at the edge of the wake with increasing Fr (e.g., Figures 14(c) and 14(d)), the influence of the average body forcing on the vertical length scales in the near wake decreases.

The lower-Fr limit to obtain a fully three dimensional near wake region[39] occurs at $Fr \simeq 4$, and this claim is supported by the near wake behavior of $L_{\sigma v}$ in Figure 15(a) and the unsteady wake contours of $w(\vec{x},t)$ in Figure 5(f). By inspection of Figure 14(c) for $2 \lesssim x \lesssim 7$, the average density is in phase with $L_{\sigma v}$, but the body force is both reduced in magnitude and appears to slip out of phase with $L_{\sigma v}$, as downstream distance increases.

In Figure 15(a), each case of $Fr \geq 4$, $L_{\sigma v}$ grows in x after $x = 2.25$ until $\{x, Nt\} \simeq \{3\,Fr/2, 3\}$. For $Fr \gtrsim 4$, the location of $x \simeq 2.25$ is the common location where it is possible to parameterize the wake widths. The near wake region begins at this location, and the region where $x \lesssim 2.25$ is referred to as the recirculation region, which is also unsteady. The length of the region is denoted by L_{rr} and is the location at which $U_o(L_{rr}) \simeq 1$. The length of this region is only weakly dependent on Fr as $L_{rr} \simeq 2.25$ for $Fr = \infty$ and $L_{rr} \simeq 2.1$ for $Fr = 4$. No attempt to parameterize this region is made because downstream characteristics in length scale behavior and flow field statistics are not compatible with the scaling form of parameterizations (Sec. IV G) available for $x \gtrsim 2.25$.

At $Fr = \infty$, a fitted parametrizations of $L_{\sigma v}$ and $L_{\sigma h}$ in the near wake between $2.25 \leq x \leq 15$ is

$$L_{\sigma v\infty} = L_{\sigma h\infty} = 0.37\,x^{0.55}, \quad 2.25 \leq x \leq 15, \tag{27}$$

where the subscript ∞ denotes the case $Fr = \infty$. Parameterizations of $L_{\sigma v}$ and $L_{\sigma h}$ in stratified near wakes should asymptote to Eq. (27) as $Fr \to \infty$. After the recirculation region, $L_{\sigma v}$ of each lower-Fr case grows at a reduced rate from the $Fr = \infty$ case. Based on the decreased growth rate of $L_{\sigma v}$ in Figure 15(a), for $Fr \geq 4$, accounting for stratification will affect the exponent in Eq. (27), where $L_{\sigma v} \sim x^{0.55 f(Fr)}$ such that $f(Fr) = 1$ for $Fr \to \infty$ and $f(Fr) \simeq 0$ when $Fr = 4$. Stratification will affect the amplitude of $L_{\sigma v}$ at $x \simeq 2.25$ due to suppression of the flow over the sphere as Fr decreases.

A numerically fitted parametrization for $L_{\sigma v}$ is given by

$$L_{\sigma vFr} = A(Fr)\,x^{\frac{0.55}{0.94+3.2/(Fr-4)}}, \quad 2.25 \lesssim x \lesssim \frac{3}{2}Fr \tag{28}$$

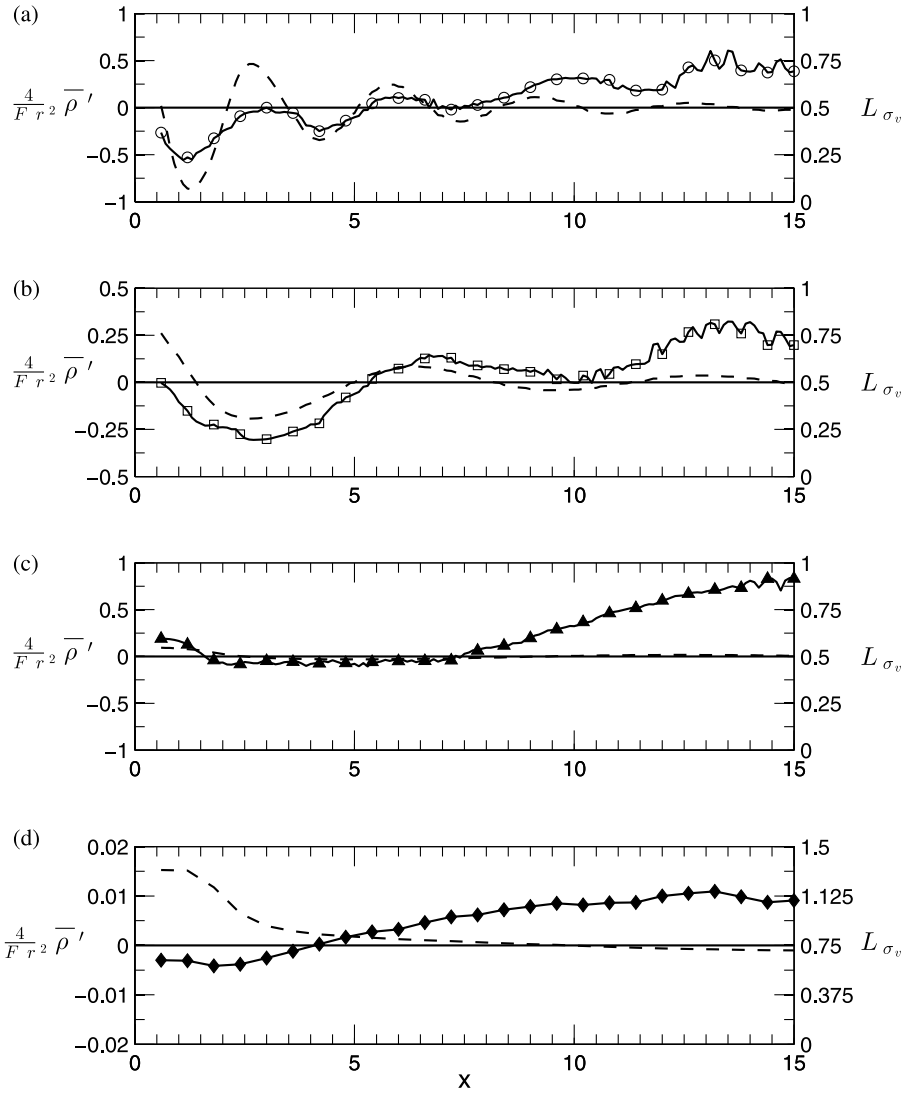

FIG. 14. Re = 1000. Comparison of average body force located at $z = L_{\sigma v}$, $y = 0$. (−−) $4\overline{\rho'}/Fr^2$ for each case and (−) is the zero axis line of the $\overline{\rho'}$ axis. Symbols indicate lines of $L_{\sigma v}$. (a) $Fr = 1$, (b) $Fr = 2$, (c) $Fr = 4$, (d) $Fr = 10$.

valid for $Fr \geq 4$, where the subscript Fr of $L_{\sigma v}$ indicates the Fr-specific case. It is worth noting that the description of $A(Fr)$ is sensitive to the function $f(Fr)$ and is empirically found to be

$$A(Fr) = 0.11\ \text{sech}\left[0.24\,(Fr - 7.42)\right] + 0.37. \tag{29}$$

Equation (28) displays an asymptotic behavior towards Eq. (27) as $Fr \to \infty$. The lower limit of $Fr = 4$ is chosen because if $Fr \lesssim 4$, $L_{\sigma v}$ does not scale similarly to the $Fr \geq 4$ cases by comparison between Figures 13 and 15(a). The change in growth of $L_{\sigma v}$ for $\{x, Nt\} \geq \{3\,Fr/2,\ 3\}$ is the beginning of the NEQ regime and is outside of the intended parametrization range. The agreement between Eq. (28) and the simulation data is qualitatively shown in Figure 15(a).

Figure 15(b) suggests that growth rates of $L_{\sigma h}$ only weakly depend on Fr in the near wake. Again, $x \simeq 2.25$ is a common starting point for significant growth in $L_{\sigma h}$. When $Fr \geq 4$, and using $Fr = 4$ as the illustrative case, $L_{\sigma h}$ does show an initial growth and changes its growth rate around $\{x, Nt\} \simeq \{3\,Fr/2,\ 3\}$.

Opposite the effects of Fr on $L_{\sigma v}$, $L_{\sigma h}$ is initially wider at $x \simeq 2.25$ with decreasing Fr. All $L_{\sigma h}$ for $Fr \geq 4$ begin at similar values directly behind the sphere as, even for strongly stratified flows, horizontal motion around the sphere is not inhibited by potential energy requirements. After

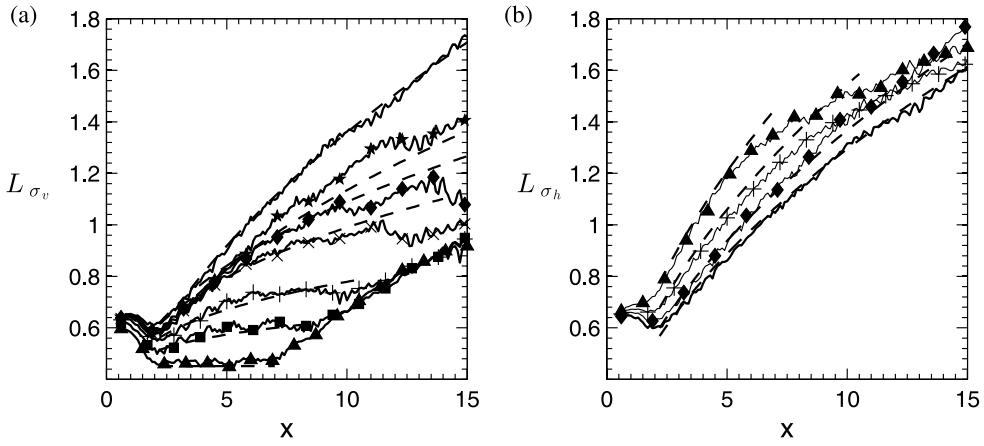

FIG. 15. Re = 1000. Half-widths of the near wake. (a) Vertical center plane at $y = 0$. (b) Horizontal center plane at $z = 0$ (every other Fr case omitted for clarity). (▲) Fr = 4, (■) Fr = 5, (+) Fr = 6, (×) Fr = 8, (♦) Fr = 10, (★) Fr = 16, (−) Fr = ∞. (−−) plotted through $Nt = 3.5$, Eq. (28) in (a), Eq. (30) in (b).

the recirculation region, at $x \simeq 2.25$, initial values of $L_{\sigma h}$ become dependent on Fr. As with $L_{\sigma v}$, $L_{\sigma h}$ should approach Eq. (27), in the $Fr \to \infty$ limit of the uniform density case. If growth rate of $L_{\sigma h}$ in the near wake is only weakly dependent on Fr, then Fr affects only the starting width of the wake at $x \gtrsim 2.25$, and a numerically fitted description is given of the form

$$L_{\sigma hFr} = B(Fr)\, x^{0.55}, \quad 2.25 \lesssim x \lesssim \frac{3}{2} Fr, \tag{30}$$

where

$$B(Fr) = 0.46 \exp(-0.31\, Fr) + 0.37 \tag{31}$$

when $Fr \geq 4$ and $\{x, Nt\} \leq \{3\, Fr/2, 3\}$. The parametrization for $L_{\sigma h}$ is plotted against the simulation results in Figure 15(b). The parametrization generally describes values of $L_{\sigma hFr}$, and deviations are related to the choice of the constant exponent in Eq. (30). Errors in estimation from the data because of this choice are typically less than 10%.

G. The near wake centerline

The centerline defect velocity, U_o, in the near wake develops with downstream distance as $U_o \sim x^{-c}$ in a uniform density fluid wake. The exponent c is commonly constant, $O(1)$, and is sensitive to the range and behavior of the data downstream of the sphere. The exponent is sensitive to the range and the methodology of the fit, where directly behind the recirculation region, U_o may behave as $U_o \sim x^{-2}$, and farther downstream, self-similar development is expected as $U_o \sim x^{-2/3}$. In the near wake, expectations of truly self-similar scaling should be abandoned because the wake is not self-similar. Nevertheless, scaling descriptions are commonly used and remain useful in describing the downstream behaviors of flow quantities.

At $Fr = \infty$, the simulation reproduces an expected decay in U_o, shown in Figure 16(a), and a simple scaling description is used to parameterize the defect velocity of the uniform density fluid wake,

$$U_o = 3.58\, x^{-1.64}, \quad 2.25 \leq x \leq 15, \tag{32}$$

where Eq. (32) is numerically fitted from the simulation data available from $x \simeq 2.25$ to $x = 15$.

In Figure 16(a), $Fr = 4$ is representative of stratification effects because U_o departs from the uniform density case immediately downstream of $x \simeq 2.25$. Upstream of $x \simeq 2.25$, which is within the recirculation region, U_o is indiscernible between the Fr cases. Between $\{x, Nt\} \simeq \{2.25, 1.1\}$ and $\{x, Nt\} \simeq \{7, 3.5\}$, departures of the stratified wakes from the uniform density case are not severe compared to the departure further downstream. After $\{x, Nt\} \simeq \{7, 3.5\}$, U_o increases very

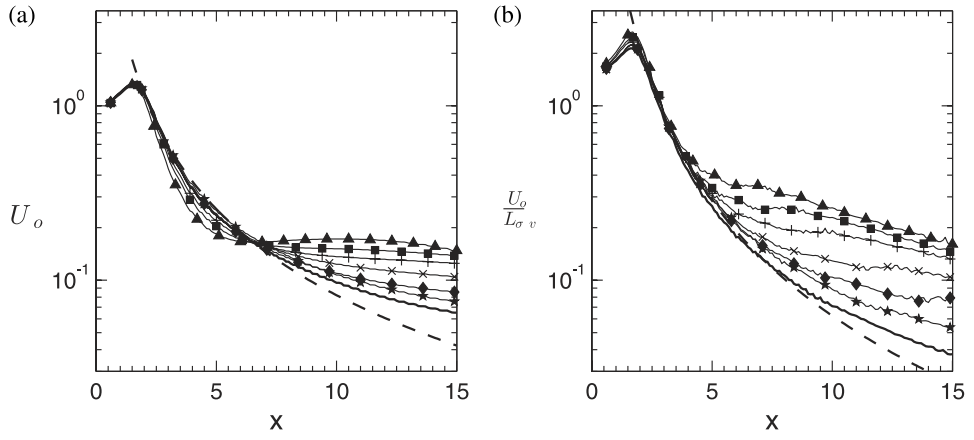

FIG. 16. Re = 1000. (a) Centerline defect velocity, U_o. (b) Normalized $U_o/L_{\sigma v}$. (▲) Fr = 4, (■) Fr = 5, (+) Fr = 6, (×) Fr = 8, (♦) Fr = 10, (★) Fr = 16, (−) Fr = ∞. (−−) Eq. (32) in (a), (−−) Eq. (34) in (b).

slightly, and after $\{x,Nt\} \simeq \{10,5\}$, it returns to decay. Similar behavior has been reported[48] for $Fr = \{3,6,10\}$ at $Re = \{3400,6900,11500\}$, respectively. At the constant $Re = 1000$, current results only indicate downstream increase of U_o in the $Fr = 4$ case, and the severity of this departure from the $Fr = \infty$ case lessens with increasing Fr as neither $Fr = 5$ nor $Fr = 6$ exhibits this increase for the same time in Nt. Spedding *et al.*[19] note that mean stream-wise velocities in the NEQ and far wake regions can be greater than that of high Fr by nearly an order of magnitude, and it is clear by maintaining a constant Re and changing Fr, as in Figure 16(a), that this is caused by stratification effects in the near wake.

It is shown in Sec. IV F that stratification influences the growth of the vertical wake width in the near wake. A stream-wise, mean local Froude number is defined as $Fr_{L_{\sigma v}} = U_o^*/(N^* L_{\sigma v}^*)$. Like the internal Fr, $Fr_{L_{\sigma v}}$ is representative of the mean energy available to a fluid particle on the wake centerline as compared to the potential energy required to vertically displace that same particle to the edge of the wake. If U_o is normalized by $L_{\sigma v}$, then that ratio may be manipulated,

$$\frac{U_o}{L_{\sigma v}} = \frac{U_o^*}{U_s^*}\frac{D^*}{L_{\sigma v}^*} = \frac{U_o^*}{N^* L_{\sigma v}^*}\frac{N^* D^*}{U_s^*} = 2\frac{Fr_{L_{\sigma v}}}{Fr}. \tag{33}$$

By Figure 16(b), regardless of Fr, $U_o/L_{\sigma v}$ collapses completely onto the uniform density case when $\{x,Nt\} \lesssim \{5,10/Fr\}$. Downstream of this point, the stratified cases begin to slightly diverge from the uniform density case until $\{x,Nt\} \simeq \{Fr,2\}$ whereafter $U_o/L_{\sigma v}$ severely departs from the uniform density case.

The data collapse in Figure 16(b) indicates that in the stratified fluid, the local ratio of available mean kinetic to potential energy requirements directly scales with internal Froude number, Fr. When $4 \le Fr \le \infty$ and $Nt \lesssim 2$, this ratio is independent of the stratification level. Additional interpretation of $U_o/L_{\sigma v}$ in the near wake is not immediately clear, although $U_o^*/L_{\sigma v}^*$ is proportional to some wake vortical time scale, and $U_o/L_{\sigma v}$ is that time scale normalized by the inverse advective time scale U_s^*/D^*, utilized previously in studies of stratified wakes.[44]

Values of $U_o/L_{\sigma v}$ in cases of $Fr = \{4,5,6,8\}$ significantly transition away from the uniform density case limit at $Nt \simeq 2$ and appear to reach a new, similar rate of decay at corresponding values $x \simeq \{8.4,9.0,9.9,12\}$ or, equivalently, $Nt \simeq \{4.2,3.6,3.3,3\}$, indicating a Fr-dependence on the length of this transition. The common departure at $Nt = 2$ of $U_o/L_{\sigma v}$ indicates that the mean flow starts to transition into the NEQ regime earlier than $L_{\sigma v}$ alone might indicate (Sec. IV F).

A straightforward modification to Eq. (32) that can parametrize U_o in the near-wake for $Fr \ge 4$ is found by using $U_o/L_{\sigma v}$, applied downstream of the recirculation region. The general collapse of the $Fr \ge 4$ data in Figure 16(b) onto the $Fr = \infty$ data for $Nt \lesssim 2$ is used to generalize the curve fit for any $Fr \ge 4$. After $Nt \simeq 2$, a virtual origin description in lieu of Eq. (32) for the NEQ region would require a shift in origin on a per-Fr basis. A modified parametrization, for the near wake, consistent

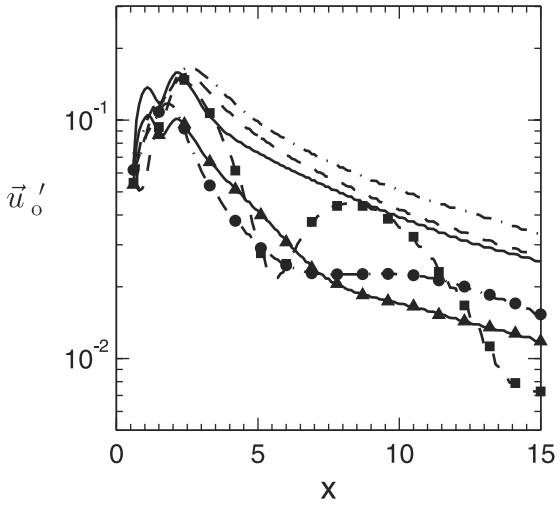

FIG. 17. Re = 1000. Anisotropy of (−) u'_o, (− · −) v'_o, (−−) w'_o in the near wake. Unmarked lines are uniform density case. The $Fr = 4$ case: (▲) u', (●) v', (■) w'.

with Eq. (32) is

$$\frac{U_{oFr}}{L_{\sigma vFr}} = 9.68\, x^{-2.19}, \quad 2.25 \lesssim x \lesssim Fr, \tag{34}$$

where the upper limit in x is equivalent to $Nt = 2$, valid for $Fr \geq 4$ and $x \leq 15$, and the subscripts Fr indicate the Froude number of the case. A larger domain could increase the accuracy of this statement for the higher Fr cases, where there is notable departure from the description provided by Eq. (34).

Descriptions of the perturbation components are presented in two ways. First, the unmanipulated data are available for all perturbation components for direct comparison. Second, the collapsed parametrized data are presented in terms of physical downstream distance x. In the cases of w'_o and ρ'_o, the data in Nt are used as a guide in an attempt to collapse the data of the near wake.

Centerline perturbation velocities for the uniform density case begin in a slightly anisotropic state for the $Re = 1000$ flow. We read peak perturbation velocity values for $\vec{u'_o} = (u'_o, v'_o, w'_o) = (0.159, 0.166, 0.156)$ at $x = (2.2, 2.5, 2.5)$ from Figure 17. While not beginning with the same energy distribution, each perturbation component in the uniform density case decreases at a similar rate. This behavior is in contrast to the behavior of u'_o, v'_o, and w'_o for the stratified $Fr = 4$ case. Qualitatively, it is also clear that the stratified perturbation velocities in the near wake do not scale in a similar fashion to each other whatsoever.

Parameterizations of velocity perturbations in uniform density case are

$$u'_o = 0.32\, x^{-0.92}, \quad 2.25 \leq x \leq 15, \tag{35}$$

$$v'_o = 0.38\, x^{-0.86}, \quad 2.25 \leq x \leq 15, \tag{36}$$

$$w'_o = 0.38\, x^{-0.94}, \quad 2.25 \leq x \leq 15. \tag{37}$$

As evident in Figure 18(a), stratification immediately affects the magnitude of u'_o in the recirculation region and subsequent values in the near wake, but it does not appear to generate a pronounced effect on the decay rate of u'_o. For $Fr = 4$, the magnitude of u'_o at $x = 2.2$ is roughly two-thirds that of the uniform density case. Only the $Fr = 4$ case hints at any significant departure from the decay rate of u'_o at $\{x, Nt\} \simeq \{7, 3.5\}$.

The Osmidov length scale in the near wake is defined as

$$l_o^* = \left(\frac{\epsilon^*}{N^{*3}}\right)^{1/2} = \left(\frac{{u'_o}^{*3}}{L^*_{\sigma v} N^{*3}}\right)^{1/2}. \tag{38}$$

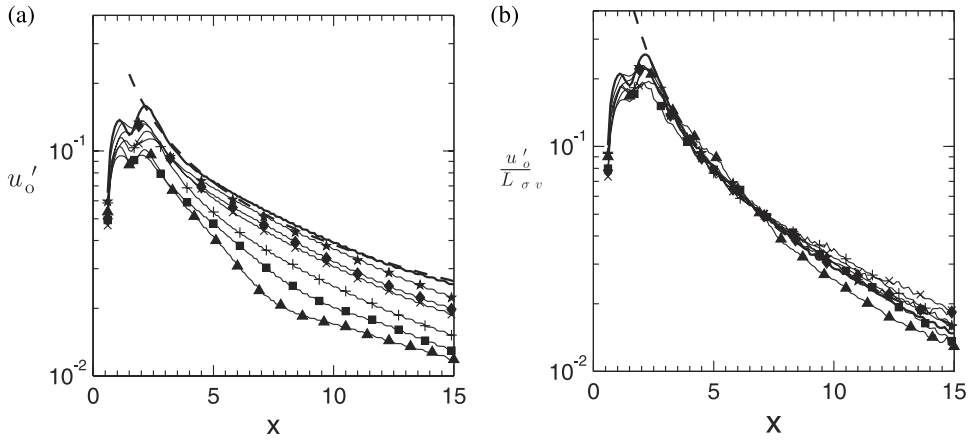

FIG. 18. Re = 1000. Centerline stream-wise perturbation velocity (a) unmodified, (b) normalized. (▲) Fr = 4, (■) Fr = 5, (+) Fr = 6, (×) Fr = 8, (♦) Fr = 10, (★) Fr = 16, (−) Fr = ∞. (−−) Eq. (35) in (a), Eq. (42) in (b).

A manipulation of Eq. (38) proceeds in the following fashion:

$$\frac{l_o^*}{L_{\sigma v}^*} = \frac{l_o}{L_{\sigma v}} = \left(\frac{\left(u'_o U_s^*\right)^3}{\left(L_{\sigma v} D^*\right)^3 N^{*3}}\right)^{1/2} = \left(\frac{u'_o}{L_{\sigma v}}\frac{Fr}{2}\right)^{3/2}, \tag{39}$$

and after rearrangement of terms provides

$$\frac{u'_o}{L_{\sigma v}} = \frac{2}{Fr}\left(\frac{l_o}{L_{\sigma v}}\right)^{2/3}. \tag{40}$$

Equation (40) indicates that the non-dimensional quantity $u'_o/L_{\sigma v}$ is representative of the ratio of the buoyant overturn length scale to turbulent integral length scale.[45] If $Fr \to \infty$ and $l_o/L_{\sigma v} \sim Fr^{3/2}$, Eq. (40) remains consistent in the unstratified limit. In a uniform density fluid, $u'_o/L_{\sigma v} = (u'_o{}^*/L_{\sigma v}{}^*)(D^*/U^*)$ is representative of an eddy turnover time normalized by the advective time scale of the flow. If a local stream-wise Froude number is defined[45] along the centerline as $Fr_{l1} = u'_o{}^*/(N^* L_{\sigma v}{}^*)$, then normalizing u'_o by $L_{\sigma v}$ is also equivalent to normalizing the local Froude number by the internal Froude number, $u'_o/L_{\sigma v} = u'_o D^*/(U_s^* L_{\sigma v}) = 2Fr_{l1}/Fr$, which is also consistent in the $Fr \to \infty$ limit, and the local perturbation kinetic energy available in the near wake will scale with Fr.

Once the normalization $u'_o/L_{\sigma v}$ is made, the near wake stream-wise perturbation velocities collapse onto the data of the uniform density case, see Figure 18(b), confirming that the local stream-wise kinetic energy scales with the potential energy requirements of particles passing over the sphere. The kink in the decay rate of $u'_o/L_{\sigma v}$ remains perceptible, yet not dramatic, as the flow enters the NEQ region. Generally, the higher the Fr, the more closely this collapse appears to follow the uniform density case for downstream values in x. There are some notable departures for the $Fr \lesssim 8$ cases of this behavior further downstream, but this may be attributed to the entry of the wake into the NEQ regime as well as edge-of-domain proximity of the damping layer.

At sufficiently high Re, if u'_o (or v'_o or w'_o) in the uniform density case, and both $L_{\sigma v\infty}$ and $L_{\sigma vFr}$ are known (i.e., by shadowgraph), then the value of the stream-wise perturbation velocity in the near wake can be predicted by

$$u'_{oFr} = u'_{o\infty}\frac{L_{\sigma vFr}}{L_{\sigma v\infty}}, \quad 2.25 \lesssim x \lesssim \frac{3}{2}Fr \tag{41}$$

valid for $Fr \geq 4$, where subscripts Fr and ∞ indicate the stratified and uniform density case values, respectively. If these data are not available, then a consistent parametrization for u'_o in the near

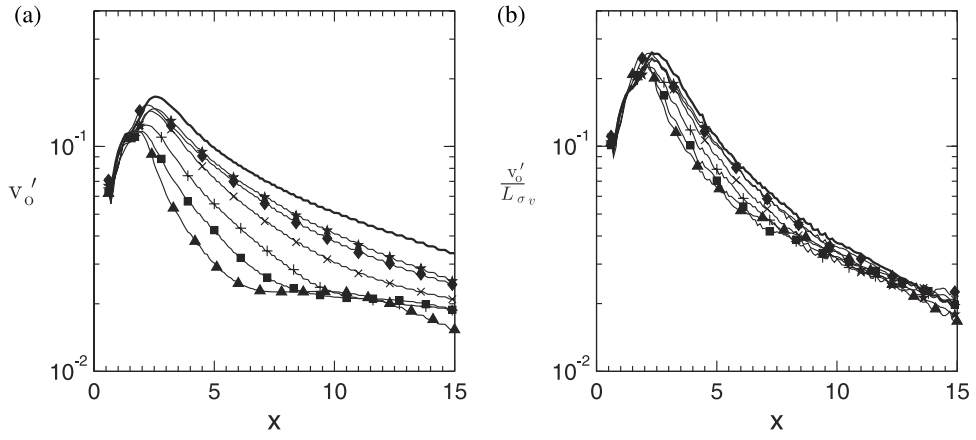

FIG. 19. Re = 1000. Centerline horizontal perturbation velocity (a) unmodified, (b) normalized. (▲) Fr = 4, (■) Fr = 5, (+) Fr = 6, (×) Fr = 8, (♦) Fr = 10, (★) Fr = 16, (−) Fr = ∞.

wake can be obtained by a fit of the uniform density case for $u'_o/L_{\sigma v}$,

$$\frac{u'_{oFr}}{L_{\sigma vFr}} = \frac{u'_{o\infty}}{L_{\sigma v\infty}} = 0.87\, x^{-1.49}, \quad 2.25 \lesssim x \lesssim \frac{3}{2}Fr, \tag{42}$$

and is valid for $Fr \geq 4$. Because of the $u'_o/L_{\sigma v}$ collapse in Figure 18(b) and Eq. (41), the subscripts of ∞ and Fr are interchangeable, and Eq. (28) may be used in place of $L_{\sigma v}$ for a full parametrization in terms of x or Nt only.

Values of v'_o in Figure 19(a) indicate that stratification can affect the decay rate of centerline perturbation values in the near wake within short distances downstream of the sphere. In the cases $Fr = \{4,5\}$, there is a notable change in decay where v'_o begins to level off further downstream from the sphere. This occurs at $x \simeq \{6, 7.5\}$ or equivalently $Nt \simeq 3$ for both $Fr = 4$ and $Fr = 5$. Following the procedure applied to u'_o, v'_o is rescaled by $L_{\sigma v}$ in Figure 19(b) such that at $x \simeq 2.25$, the values of the uniform density case and stratified cases for $v'_o/L_{\sigma v}$ reach a closer agreement. Similar to u'_o, this is equivalent to normalizing a lateral, local Froude number $Fr_{l2} = {v'_o}^*/(N^* L^*_{\sigma v})$ by the internal Froude number.

This rescaling, seen in Figure 19(b), is insufficient to collapse the data in the near wake region for v'_o. An attempt at correction to the collapse is made by the use of a fitted asymptotic function such that parameterizations of v'_o, for $x \gtrsim 2.25$, scale with the uniform density case. The fitted form of the asymptotic function, $f_v(Fr)$, is

$$f_v(Fr) = 0.26 \tanh\left(0.39\frac{Fr}{2}\right) \tag{43}$$

and asymptotes to 1 as $Fr \to \infty$. It is reiterated that the parametrizations are intended to be applied for $Fr \geq 4$, which is also inherent to the parametrization through Eq. (42). The behavior of Eq. (43) as $Fr \to 0$ is not necessarily representative of the wake behavior. The parametrization that is consistent with Eq. (36) becomes

$$\frac{v'_{oFr}}{L_{\sigma vFr}} = 3.95\, f_v(Fr)\, x^{-1.43}, \quad 2.25 \lesssim x \lesssim \frac{3}{2}Fr \tag{44}$$

and Fr has replaced the ∞ subscript in Eq. (44) through the same reasoning applied to u'_o. This parametrization is shown in Figure 20 where the near wake values and Eq. (44) are in perfect agreement.

Out of all perturbation velocity values along the centerline, w'_o is the most dramatically affected by stratification. Figure 21(a) indicates significant, oscillatory behavior in w'_o within short downstream distances from the sphere, even at a moderate values of Fr, such as $Fr = 8$. Furthermore, the curvature of the initial decay for lower Fr is inflected from that of the u'_o or v'_o quantities. It appears from Figure 21(a) that w'_o will always depart from the uniform density case

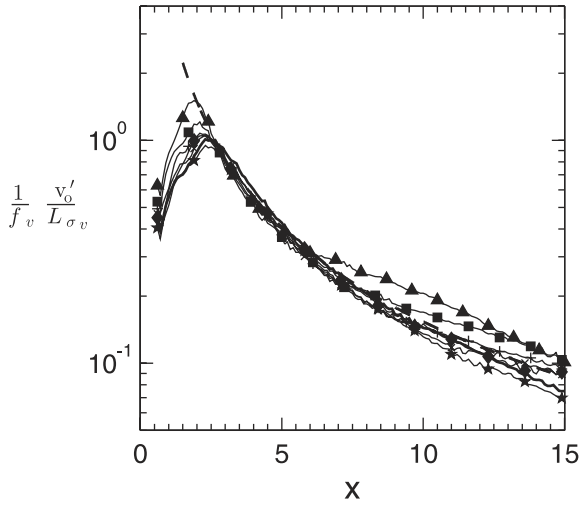

FIG. 20. Re = 1000. Collapse of $v'_o/L_{\sigma v}$ by Eq. (43). (▲) Fr = 4, (■) Fr = 5, (+) Fr = 6, (×) Fr = 8, (♦) Fr = 10, (★) Fr = 16, (−) Fr = ∞, (−−) Eq. (44).

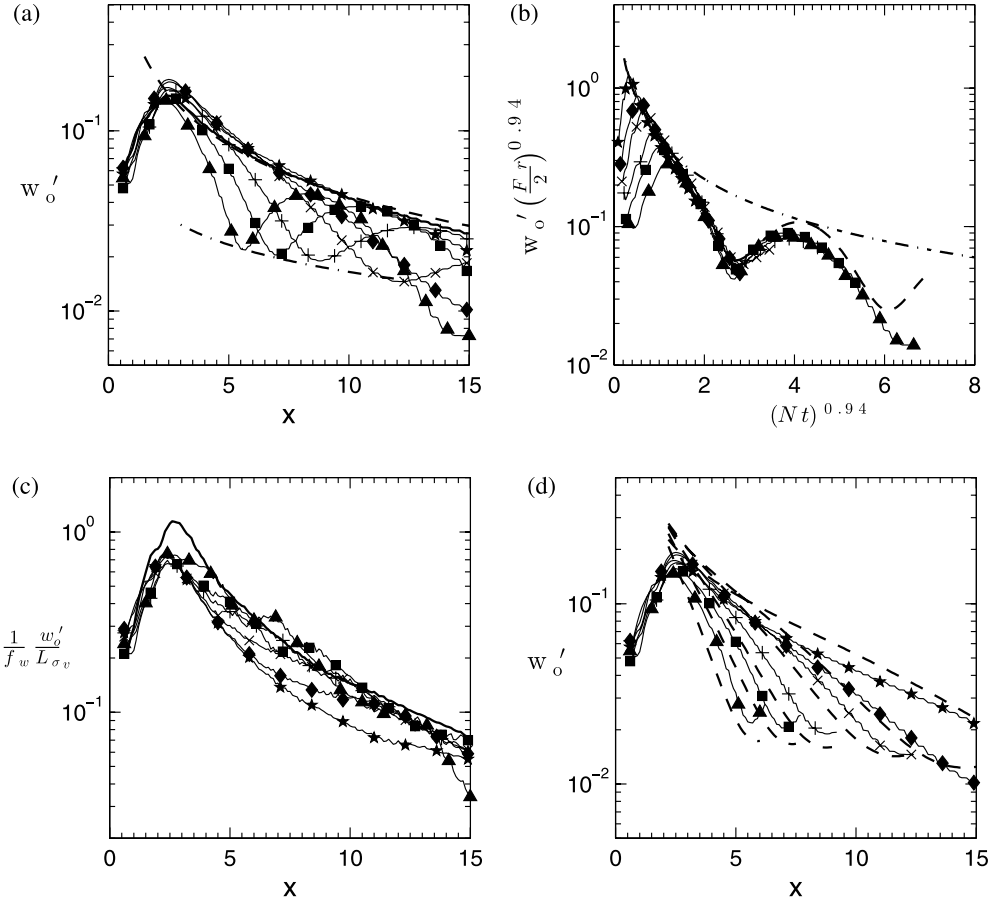

FIG. 21. *Re* = 1000; (▲) Fr = 4, (■) Fr = 5, (+) Fr = 6, (×) Fr = 8, (♦) Fr = 10, (★) Fr = 16, (−) Fr = ∞. (a) Highly oscillatory nature of w'_o, (−−) Eq. (37), (−·−) Eq. (45). (b) Collapse of w'_o in *Nt*, (−·−) $\sim Nt^{-0.94}$, (−−) $\sim f_w Nt^{-0.94}$. (c) Reduced oscillations in perturbation velocity. (d) Parametrized vertical perturbation velocity, (−−) Eq. (48).

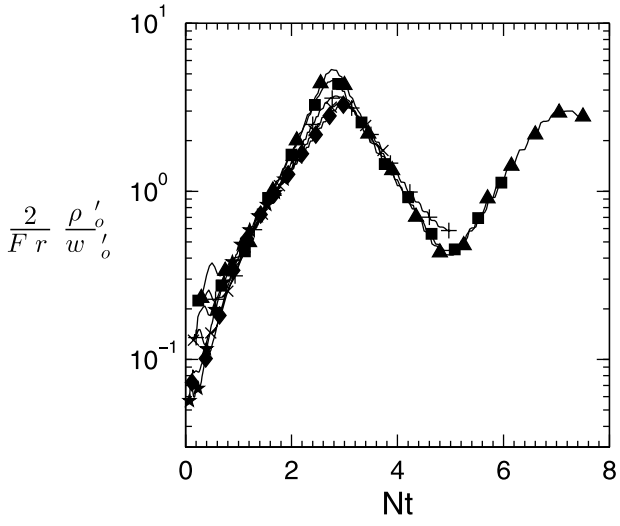

FIG. 22. Re = 1000. Ratio of centerline density perturbation ρ'_o to vertical velocity perturbation w'_o.

for low-to-moderate Fr values at some x and Fr pairing. The first visible valley of w'_o occurs at locations $x \simeq \{6, 7.5, 9, 12\}$ for $Fr = \{2, 2.5, 3, 4\}$, respectively, or at $Nt \simeq 3$ for all these Fr cases.

An estimate of Fr value where this oscillatory behavior could be considered negligible is possible. The valleys are described by

$$w'_o|_{Nt=3} = 0.033\, x^{-0.54} \tag{45}$$

for $Fr \geq 4$, where $w'_o|_{Nt=3}$ indicates the recorded value of w'_o in the first valley. The $Fr = 10$ case is not included in the parametrization due to the $Nt = 3$ condition being coincident with the onset of the damping layer. The intersection of Eqs. (37) and (45) would occur at $x \simeq 450$. Based on the visible trend, the case at which stratification becomes negligible in the near wake would also occur within a negligible valley at $Nt \simeq 3$. This negligible reduction correlates with a $Fr \simeq 150$. Naturally, this prediction is sensitive to the accuracy of the description in both Eqs. (37) and (45). With a larger domain, it may be possible to obtain a better estimate, but perhaps, it is reasonable to suggest that when $Fr \sim O(100)$, the differences between a stratified flow and a uniform density flow are negligible.

The valleys of w'_o at $Nt = 3$ are located at the same location of the local maximum of the collapsed ρ'_o/w'_o at $Nt = 3$ in Figure 22. Potential energy in a linearly stratified fluid is associated with ρ'_o because ρ'_o is representative of the vertical displacement of fluid particles away from their equilibrium position. The vertical turbulent kinetic energy is associated with w'_o. Thus, Figure 22 can be seen as representative of the centerline ratio of turbulent potential energy to vertical turbulent kinetic energy. The valleys in w'_o of Figure 21(a) are representing the process of transferring vertical turbulent kinetic energy into turbulent potential energy. As the values of w'_o increase out of the valleys, some of the turbulent potential energy is being converted back into vertical turbulent kinetic energy and vice versa for the descent of w'_o into a valley.

Both u'_o and v'_o behave as the uniform density case when $Fr \to \infty$, and Eqs. (42) and (44) reflect this condition. Any parametrization of w'_o should asymptote in a similar fashion. Oscillations are not likely removed by normalizing w'_o by $L_{\sigma v}$ alone because, as seen in Figure 15(a), there are no notable oscillations of $L_{\sigma v}$ for $Fr \geq 4$ that would account for such large amplitude oscillations in w'_o. Oscillations could be smoothed if the quantity w'_o is normalized by the "correct" choice of oscillatory function. Because of the form chosen to describe w'_o in Eq. (37), a parametrized equation is sought in the form

$$w'_o\left(\frac{Fr}{2}\right)^{0.94} = f_w\,(Fr, Nt)\,(Nt)^{-0.94}, \tag{46}$$

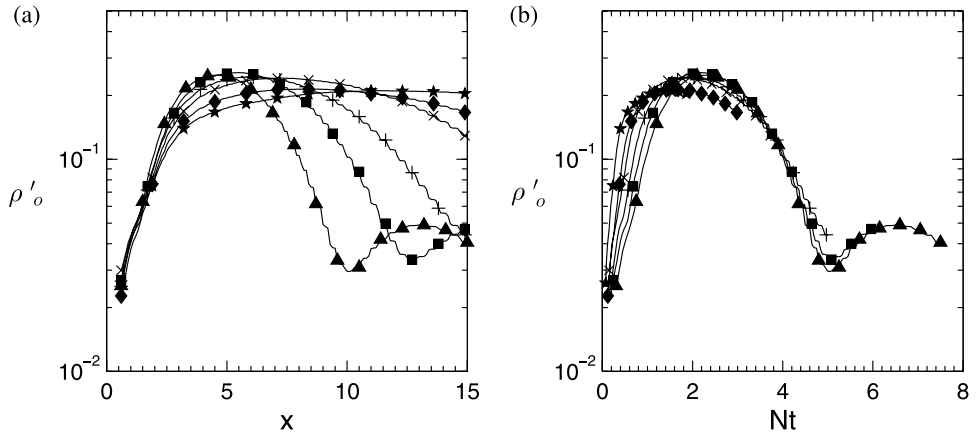

FIG. 23. $Re = 1000$. Centerline density perturbation. (▲) Fr = 4, (■) Fr = 5, (+) Fr = 6, (×) Fr = 8, (♦) Fr = 10, (★) Fr = 16.

where $f_w(Fr,Nt)$ is some oscillatory function dependent on Fr and Nt that compliments the decay rate in time and should asymptote to unity when $Fr \to \infty$. The final form of Eq. (46) is expected to translate consistently into x, and because f_w asymptotes to unity as $Fr \to \infty$, w'_o must be multiplied by $(Fr/2)^{-0.94}$, as done in Figure 21(b). Like f_v, there is no particular restriction on f_w as $Fr \to 0$ because $Fr = 4$ is intended to be the limiting case.

When viewed in Nt through Figure 21(b), $w'_o(Fr/2)^{0.94}$ is collapsed and the decay appears independent of Fr for $4.5/Fr \lesssim Nt \simeq 3$, at which point there is growth in Nt until $Nt \gtrsim 4$ when there is a return to decay. The proposed form for f_w is then

$$f_w(Fr,Nt) = 0.15\left[2 + \sin\left(1.16\frac{\pi}{2}(Nt)^{0.94}\right)\right]. \tag{47}$$

A description of $w'_o/L_{\sigma v}$ in the $Fr = \infty$ case provides an estimate of the stratified behavior of $w'_o/(f_w L_{\sigma v})$ by Figure 21(c). A parametrization that describes $w'_o/L_{\sigma v}$ at $Fr = \infty$ is then

$$\frac{w'_{oFr}}{L_{\sigma vFr}} = \frac{w'_{o\infty}}{L_{\sigma v\infty}} = 2.9\, f_w(Fr,x)\, x^{-1.49}, \quad 2.25 \le x \le \frac{3}{2}Fr \tag{48}$$

which is a parametrization of the vertical velocity coefficient and Eq. (28) may be used for a parametrization of w'_o purely in x. This parametrization is shown in Figure 21(d) where Eq. (48) tends to over or under predict the Fr cases controlled by the generated collapse seen in Figure 21(c).

Centerline values of ρ'_o for the near wake are presented in Figure 23, where views of ρ'_o show a relative independence from Fr for $x \lesssim 2.25$, which is within the recirculation region. The development of ρ'_o is physically described by a quick growth within and behind the recirculation region, followed by an oscillatory decay. This is related to the transfer of energy as previously described through Figure 22. When viewed in x, there is no obvious simple correlation between the value of the magnitudes and location of the peaks between the various Fr cases. Analysis of ρ'_o in Nt, as in Figure 23(b), may aid in the parametrization of ρ'_o because it appears that $Nt \simeq 5$ may be the time at which ρ'_o is at a local minimum for all cases of $Fr \ge 4$.

Unfortunately, domain limits prohibit utilizing the trends of the higher Fr cases to generate an oscillatory non-linear parametrization of ρ'_o in Nt alone, as attempted for w'_o. Results for the $Fr = 4$ case in the near wake lead to use of an empirical nonlinear parametrization in Nt of the form

$$\rho'_o = 0.116\left[1 + 2.4\sin^2(0.32Nt)\right](Nt)^{1.26}\exp(-0.64\,(Nt)), \quad 0.3 \le Nt \lesssim 4 \tag{49}$$

which is included in Figure 24 against the simulation result of ρ'_o for $Fr = 4$. The result of this parametrization is quite representative of the behavior of ρ'_o in the near wake and the form of Eq. (49) is chosen based on the behaviors of ρ'_o across the various cases in Fr in Figure 23(b). The severity of the oscillations appears to decrease based on the $Fr = \{4,5,6\}$ cases at $Nt \simeq 5$ in Figure 23(b), although the $Nt = 5$ condition for the $Fr = 6$ case is located at the onset of the damping layer.

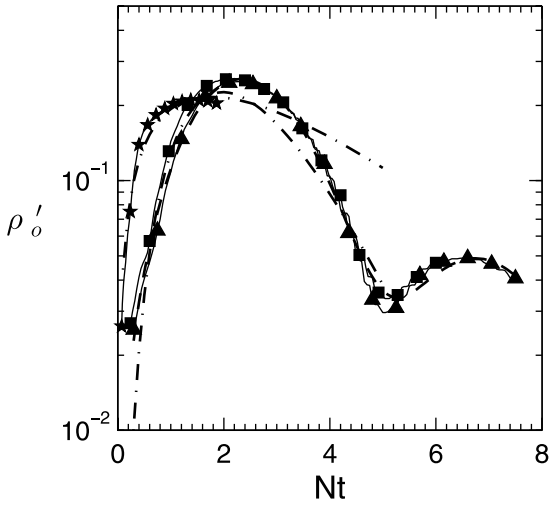

FIG. 24. $Re = 1000$. Comparison of simulation result to parametrization of ρ'_o. (▲) Fr = 4, (■) Fr = 5, (★) Fr = 16, (−−) Eq. (49), (− · −) Eq. (50).

The tendency towards a decrease in severity in the oscillations of ρ'_o suggests that, in the near wake, the sinusoidal term of Eq. (49) may be removed for a higher Fr fluid. For $Fr \geq 5$, the description in x can be empirically fitted as

$$\rho'_o = 0.056 \tanh\left(\frac{Fr}{6}\right) x^{17.5Fr^{-1}} \exp\left(-15Fr^{-2}\right), \quad 2.25 \leq x \lesssim \frac{3}{2}Fr \tag{50}$$

and this is also shown, translated into Nt, in Figure 24 for the $Fr = 5$ and $Fr = 16$ cases. For $Fr \geq 5$, Eq. (50) appears as a good, simple alternative to the form of Eq. (49) for the higher Fr cases, although for the $Fr \to \infty$ case, Eq. (50) results in a negligible value. This is not of concern as the buoyant body force in Eq. (1) is identically zero as $Fr \to \infty$.

H. The near wake in the vertical and horizontal centerplane

The near wake of the sphere at $Re = 1000$ for moderate to high Fr is fully three-dimensional and anisotropic. A description of the near wake in the vertical and horizontal planes is useful in completing descriptions of the near wake. Because the gravity vector is implicitly present as $-g\hat{k}$ in Eq. (1), and the sphere is an axially symmetric body, there are two planes about which the statistical descriptions are expected to be symmetric which are the planes shown in Figure 6(a).

The vertical centerplane is a plane of symmetry because gravity does not contain a horizontal bias in Eq. (1), and the horizontal centerplane is a plane of symmetry because particles should flow equally over and under the sphere because, in a linearly stratified fluid, there is no vertical bias in the buoyant body forces about the horizontal centerplane. Unless otherwise stated, all references to the vertical plane and horizontal plane refer to the respective centerplanes of symmetry.

At $Re = 1000$, the uniform density fluid flow around the sphere and the wake is assumed axisymmetric such that variance in the statistical description of the flow field is also invariant to the rotation of the y or z axes about the wake centerline. Any directional bias in the wake caused by choice of Re in the uniform density fluid would likely manifest itself in asymmetric vertical and horizontal velocity field distributions between the vertical and horizontal planes about the centerline. The same vertical and horizontal planes used to describe the stratified fluids in Figure 6(a) are also used to describe the near wake for the uniform density fluid.

The general form used to parametrize the wake in the vertical plane is of the form

$$\left.\frac{q(x,z)}{q_o(x)}\right|_{Fr} = \exp\left[-\frac{(z/L_{\sigma v} - B_z)^2}{C_z^2} + \frac{B_z^2}{C_z^2}\right] + \exp\left[-\frac{(z/L_{\sigma v} + B_z)^2}{C_z^2} + \frac{B_z^2}{C_z^2}\right] \tag{51}$$

and, likewise, a description in the horizontal plane is of the form

$$\left.\frac{q(x,y)}{q_o(x)}\right|_{Fr} = \exp\left[-\frac{\left(y/L_{\sigma h}-B_y\right)^2}{C_y^2}+\frac{B_y^2}{C_y^2}\right] + \exp\left[-\frac{\left(y/L_{\sigma h}+B_y\right)^2}{C_y^2}+\frac{B_y^2}{C_y^2}\right], \tag{52}$$

where $q(x,z) = q(x, y = 0, z)$, or $q(x,y) = q(x, y, z = 0)$, is a flow field variable, q_o represents its centerline value at $q(x, y = 0, z = 0)$, and the subscript Fr indicates the specific internal Froude number. At $Re = 1000$, the coefficients B_z, C_z, B_y, and C_y are tunable for Eqs. (51) and (52) and are dependent on Fr and the variable, q, of interest. By allowing separate descriptions in the vertical and horizontal planes, it is possible to discuss asymmetry in the near wake that exists within the vertical and horizontal planes.

In obtaining the coefficients for Eqs. (51) and (52), the physical coordinates of the horizontal and vertical planes are also normalized by the appropriate half-width length scale, $L_{\sigma v}$ for z and $L_{\sigma h}$ for y. The variance of the data for the uniform density and stratified near wake cases reasonably collapses for $2.25 \leq x \lesssim Fr$, where the upper limit is equivalent to $Nt = 2$. Because of the damping layer, $Fr = 10$ is the highest stratified simulation that reaches $Nt = 2$ prior to the onset of the damping layer at $x = 15$. The $Fr = \infty$ case is only limited by the onset of the damping layer. After the data collapse, the data are numerically fitted to the descriptions of Eq. (51) or (52), depending on the plane.

Following this procedure, Figure 25 contains the best-fit curves of the near wake for selected values of parameter Fr. From the numerically fitted curves of the $Fr = \infty$ case, it appears that assumptions of the axisymmetric wake are satisfied, with only minor asymmetry in the fitted profiles compared between Figures 25(e) and 25(f) for v'/v'_o and Figures 25(g) and 25(h) for w'/w'_o. With higher Re, the variance between fitted profile widths in the uniform density case should decrease. While these arguments are based on best-fit curves, Sec. IV I will also confirm that the $Fr = \infty$ simulation data can be considered axially symmetric.

In comparison between the vertical and horizontal planes, the profiles are wake-width normalized, and in the uniform density case, the length scales are identical (Eq. (27)) such that profile widths directly compare to symmetry of the near wake width. This is not true for the stratified cases, and although profiles may appear to have similar profile widths in the vertical and horizontal planes, the quantities are physically wider in width than height (Figures 6(b) and 15). Additionally, direct comparisons across Fr cases through Figure 25 are difficult because each flow field variable is normalized by its centerline quantity, which by Sec. IV G is shown to vary with parameter Fr. Quantitative commentary on the physical processes involved in creating the near wake behavior is desirable. This would require an additional formal analysis using each individual terms of Eqs. (1) and (3) and is reserved for future investigations. Qualitative commentary remains possible for some of the defining features of the wake in the vertical and horizontal centerplanes, and the distribution of these quantities at various Fr can be compared.

In the vertical centerplane of Figure 25(a), stratification does not appear to have any pronounced effect on the mean stream-wise velocity distribution within the near wake. In the horizontal centerplane, Figure 25(b), the mean stream-wise velocity tends towards a wider distribution throughout the wake as Fr decreases. At $Fr = 4$, the mean stream-wise velocity reaches its maximum value off-centerline which is quite different from the higher Fr cases. In the vertical plane, the stream-wise velocity perturbation quantities, u'/u'_o, in Figure 25(c) are higher, relative to their centerline values, than in the uniform density case, but the vertical plane velocity v'/v'_o distributions are unaffected by the presence of stratification (Figure 25(e)). The variance of the stratified case values of w'/w'_o in Figure 25(g) is slightly less than the uniform density case. It appears that once the fluid is stratified, the distribution of w'/w'_o between Fr cases in the near wake appears generally unaffected, relative to the centerline values, by the severity of stratification. All horizontal plane velocity perturbation quantities (Figures 25(d), 25(f), and 25(h)) contain maximum normalized values at off-centerline locations, and in relation to the respective centerline values, the value of this maximum increases as Fr decreases.

For the stratified cases, the centerline-normalized perturbation density profiles in Figures 25(i) and 25(j) display an axial asymmetry between vertical and horizontal planes when comparing their

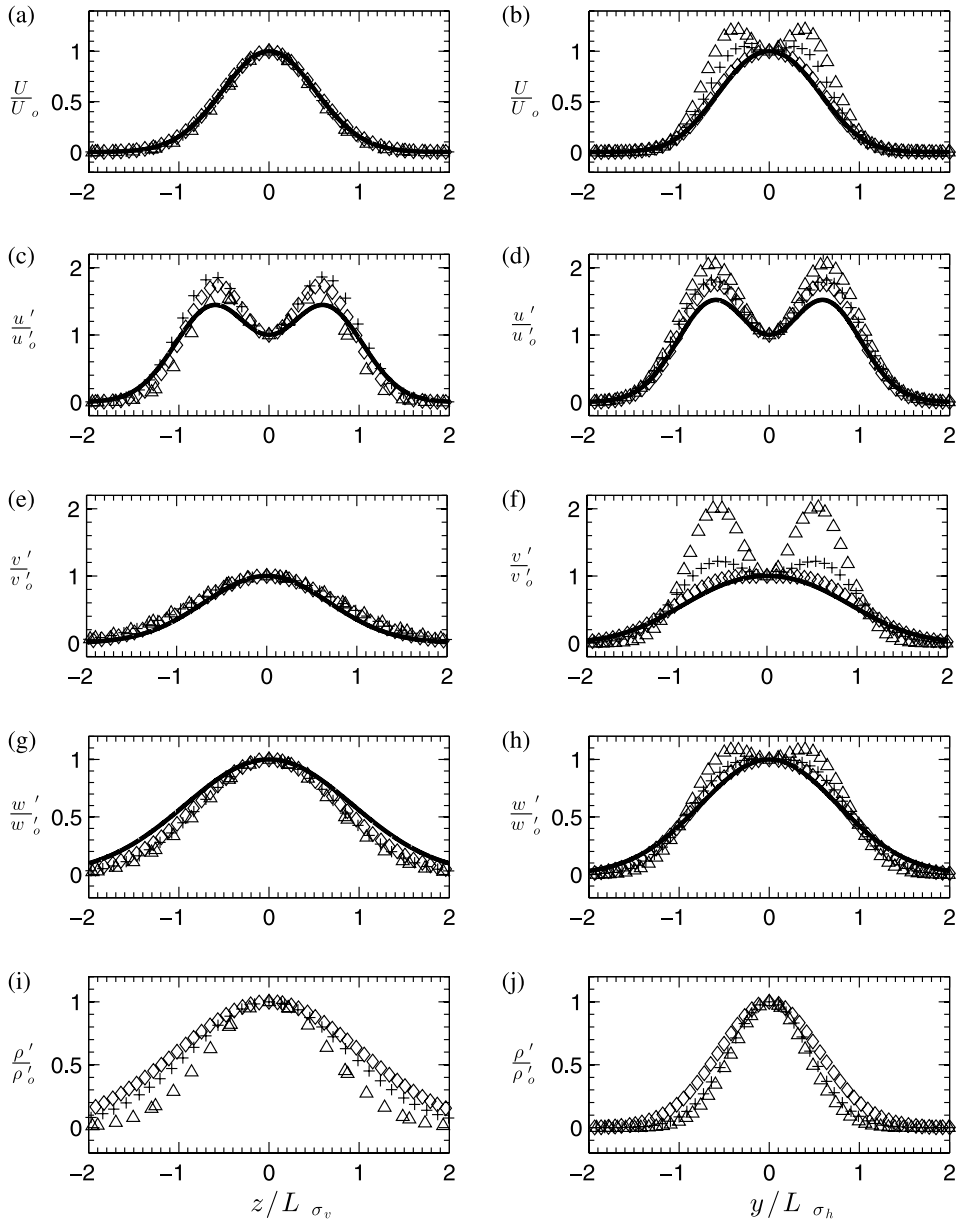

FIG. 25. Re = 1000. Numerical fit of time-averaged data for $2.25 \le x \le Fr$. Left column is on $y = 0$ plane. Right column is on $z = 0$ plane. (△) Fr = 4, (+) Fr = 6, (◊) Fr = 10, (−) Fr = ∞.

profile widths. In the vertical plane, as *Fr* increases, the variance of the profile in the vertical plane increases and appears to create a "front" of ρ'/ρ'_o. This is likely due to the ease of displacing a particle in a lightly stratified fluid because as *Fr* increases, the ratio of available kinetic energy to the energy required for a vertical fluid displacement also increases. The profile of ρ'/ρ'_o maintains its horizontal distribution within the near wake fairly regularly across the stratified cases, similar to what is seen in w'/w'_o in Figure 25(h). If ρ' is generated primarily through vertical motions, it is not surprising that the horizontal distribution of ρ'/ρ'_o in the wake is relatively unaffected by stratification.

The coefficients of Eqs. (51) and (52) that are obtained from numerically fitting the data to each curve in Figure 25 are available in Tables II and III, respectively. For cases of *Fr* that are not explicitly listed in Tables II and III, linear interpolation between entries may be used. If the

TABLE II. Coefficients for vertical parametrizations in Figures 25(a) and 25(c)–25(f). n/a: not applicable.

	U/U_o		u'/u'_o		v'/v'_o		w'/w'_o		ρ'/ρ'_o	
Fr	B_z	C_z	B_z	C_z	B_z	C_z	B_z	C_z	B_z	C_z
4	0.00	0.69	0.54	0.50	0.00	1.18	0.00	1.02	0.00	0.95
6	0.00	0.72	0.62	0.54	0.00	1.16	0.00	1.07	0.00	1.24
10	0.00	0.74	0.58	0.52	0.00	1.08	0.00	1.12	0.00	1.43
∞	0.00	0.73	0.62	0.60	0.00	0.98	0.00	1.31	n/a	n/a

TABLE III. Coefficients for horizontal parametrizations in Figures 25(b), 25(d), 25(f), 25(h), and 25(j). n/a: not applicable.

	U/U_o		u'/u'_o		v'/v'_o		w'/w'_o		ρ'/ρ'_o	
Fr	B_y	C_y	B_y	C_y	B_y	C_y	B_y	C_y	B_y	C_y
4	0.41	0.44	0.63	0.53	0.55	0.47	0.47	0.56	0.00	0.58
6	0.37	0.46	0.63	0.56	0.57	0.62	0.46	0.65	0.00	0.64
10	0.32	0.55	0.61	0.54	0.54	0.76	0.44	0.76	0.00	0.79
∞	0.29	0.59	0.61	0.58	0.47	0.91	0.01	1.08	n/a	n/a

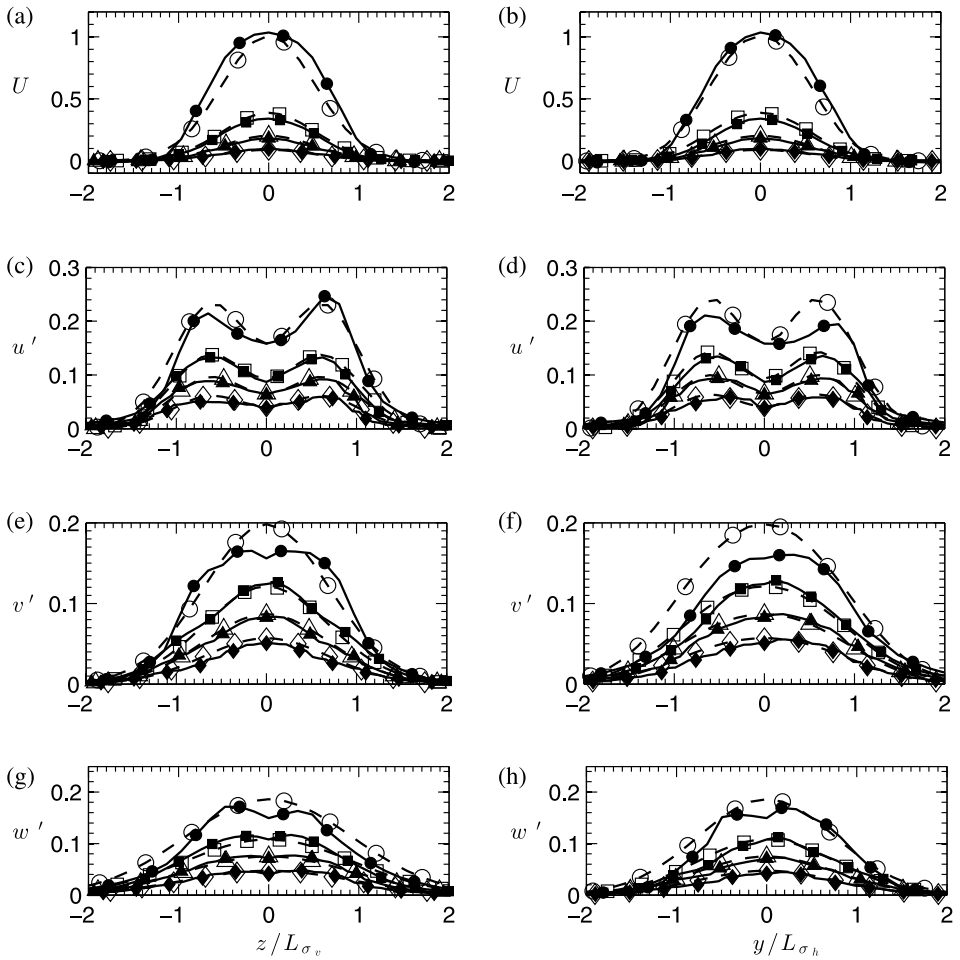

FIG. 26. Re = 1000, Fr = ∞. Parametrizations versus simulation data. (−) w/ filled symbols are simulation data, (−−) w/ open symbols are parametrizations. (●) $x = 2.25$, (■) $x = 3$, (▲) $x = 6$, (♦) $x = 9$.

stratified case of interest requires $Fr > 10$, substituting a value of $Fr \simeq 30$ for the $Fr = \infty$ value is recommended in determining high-Fr interpolated values. For future simulations interested in initialization of the near wake without accounting for the sphere, fully three dimensional profiles can be generated by interpolation between Eqs. (51) and (52).

I. Parametrizations vs. simulation data at Re = 1000

Two examples of the effectiveness of the $Re = 1000$ near wake parametrizations are given; one for $Fr = \infty$ and the other for $Fr = 6$. In Figures 26 and 27, flow field quantities described by Eqs. (34), (42), (44), and (48), as well as (50) in the $Fr = 6$ case, are compared against the time-averaged quantities obtained directly from the simulations.

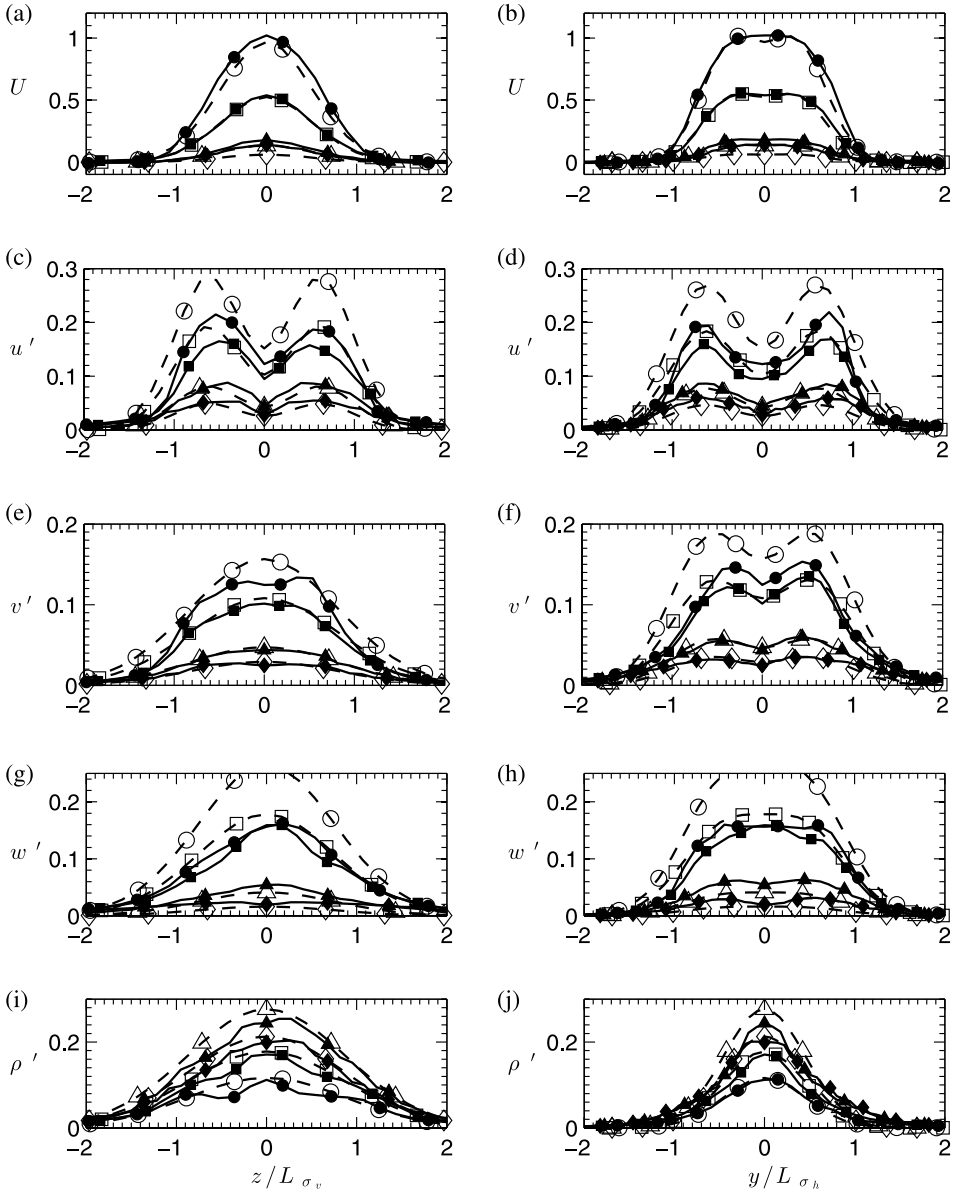

FIG. 27. Re = 1000, Fr = 6. Parametrizations versus simulation data. (−) w/ filled symbols are simulation data, (−−) w/ open symbols are parametrizations. (●) $\{x, Nt\} = \{2.25, 0.75\}$, (■) $\{x, Nt\} = \{3, 1\}$, (▲) $\{x, Nt\} = \{6, 2\}$, (♦) $\{x, Nt\} = \{9, 3\}$.

By Figures 26(a)-26(h), at $Fr = \infty$, the claim of axisymmetry (Sec. IV H) produced in the simulation is reasonable. Despite some overprediction of v' at $x \simeq 2.25$, the parametrizations appear to replicate the simulation flow field well. Figures 27(a)-27(j) also indicate that the parametrizations of the stratified $Fr = 6$ case generally reproduce the vertical and horizontal flow fields when $\{x, Nt\} > \{2.25, 2.25(Fr/2)^{-1}\}$. As expected, parametrizations of w'/w'_o in Figures 27(g) and 27(j) are not quite as accurate as those for other velocity components, and this is related to the relatively coarse collapse of the centerline quantities seen in Figure 21(c). The parametrized density perturbation quantities, ρ', in Figures 26(i) and 26(j) reproduce the simulation results fairly well.

V. CONCLUSION

Simulations have been performed for a wide range of Fr values at both $Re = 200$ and $Re = 1000$. Improvements over the prior numerical investigation[4] at $Re = 200$ of stratified fluid are shown, and the internal lee wavelengths are found to be unaffected by the coherent vortex shedding at low Fr. The internal lee waves are correlated with the average density field. At $Re = 1000$, the simulations provide quantitative descriptions of the velocity and density field behind the sphere and indicate that the internal wave field (Figure 5) for $Fr \geq 1$ is not qualitatively affected by differences between $Re = 200$ and $Re = 1000$. Internal waves were not detected by inflections of $W(\vec{x}, t)$ anywhere in the free stream for $Fr \geq 5$. A full description of the major field components is described for $4 \leq Fr \leq \infty$ at a single $Re = 1000$ and appears to be the first full component field data set available in the stratified near wake.

A detailed investigation explained the inherent differences between statistical results between an experimental (i.e., DPIV) setup and a numerical investigation due to the different methodologies in statistical collection techniques. The "tails" of the data at low Fr are artifacts of the averaging techniques being applied within the unsteady near wake region. Space and time averages are shown as not equivalent in the stratified near wake. Removing the steady lee wave field velocity components (i.e., $w(\vec{x})$ in Figure 5) from the velocity field before the spatial integration would likely remove the non-zero asymptote, and the temporal variation could be smoothed through an averaging of windowed data subsets, as done for the simulation results in Figure 7(b). Some leeway should be expected in directly comparing between experimentally and numerically collected field data in the near wake of stratified fluids when different averaging techniques are employed.

The beginning of the unsteady near wake region starts at $x = L_{rr} \simeq 2.25$ when $Fr \geq 4$. Based on the analysis of $L_{\sigma v}$, $L_{\sigma h}$, mean stream wise velocity, and the perturbation quantities for $Fr < O(100)$, there is no region in the wake of the sphere where buoyancy will not affect the near wake at $Re = 1000$. The near wake region in stratified fluids should be given a better descriptor than the "3D near wake" lest the statistical behavior of the stratified near wake becomes erroneously synonymous with the behavior of the near wake of a uniform density fluid.

Future simulations may attempt to account for the sphere within the computational domain in their own particular way, and a self-contained point of comparison is now available for unsteady stratified flows. Other numerical simulations can initialize physically close to the sphere without having to actually account for the sphere explicitly within the computational domain by using the given parametrizations. The benefits of doing this may result in achieving a higher correlation of simulation-to-physical downstream distances from the sphere, spatially varying initial conditions that account for the density field, and shorter initial simulation relaxation times.[9]

Making this claim, we recognize there are two competing requirements in "proper" initialization of simulations within the near wake that do not explicitly account for the sphere. The first is maintaining a total coherence of the near wake, which would likely require full-interpolations between near wake domains.[6] This is not necessarily a trivial task between various grid geometries especially with respect to the sensitivities to interpolation errors of highly accurate non-dissipative numerical methods. Second, there is likely a practical requirement to quickly implement the initial conditions into existing numerical schemes without major modification to the previously initialization procedures.

The parametrizations offer a relative optimum by spatially varying along the wake centerline while varying in the horizontal and vertical directions to account for downstream development of the near wake. They can be easily implemented into a numerical simulation while leaving the existing initialization scheme relatively intact, and an implementation guide is provided in the Appendix for convenient reference.

ACKNOWLEDGMENTS

This work was supported by the Office of Naval Research, administered by R. Joslin, whose support is gratefully acknowledged. One of the authors (J.A.D.) was partially supported by the NSF Grant No. 1233160. The USC HPCC generously provided the parallel computing resources required to generate the full-field data sets. The MATLAB Curve Fitting Toolbox (v3.2) software was used to aid in the parametrization of the near wake.

APPENDIX: PROCEDURE TO INITIALIZE SPHERE-LESS SIMULATIONS

The procedure as well as relevant equations is reproduced here for convenience. At each node, the following steps take place.

Step 1. Calculate $L_{\sigma v}$ and $L_{\sigma h}$ by

$$L_{\sigma vFr} = A(Fr)\, x^{\frac{0.55}{0.94+3.2/(Fr-4)}}, \qquad 2.25 \lesssim x \lesssim \frac{3}{2}Fr, \tag{A1}$$

$$L_{\sigma hFr} = B(Fr)\, x^{0.55}, \qquad 2.25 \lesssim x \lesssim \frac{3}{2}Fr, \tag{A2}$$

$$A(Fr) = 0.11\ \operatorname{sech}\left[0.24\,(Fr - 7.42)\right] + 0.37,$$
$$B(Fr) = 0.46 \exp\left(-0.31\,Fr\right) + 0.37.$$

Step 2. Use values of $L_{\sigma v}$ and $L_{\sigma h}$ from Step 1 to calculate U_o, ${u'}_o$, ${v'}_o$, ${w'}_o$, and ${\rho'}_o$ by

$$\frac{U_{oFr}}{L_{\sigma vFr}} = 9.68\, x^{-2.19}, \qquad 2.25 \lesssim x \lesssim Fr, \tag{A3}$$

$$\frac{{u'}_{oFr}}{L_{\sigma vFr}} = 0.87\, x^{-1.49}, \qquad 2.25 \lesssim x \lesssim \frac{3}{2}Fr, \tag{A4}$$

$$\frac{{v'}_{oFr}}{L_{\sigma vFr}} = 3.95\, f_v(Fr)\, x^{-1.43}, \qquad 2.25 \lesssim x \lesssim \frac{3}{2}Fr, \tag{A5}$$

$$\frac{{w'}_{oFr}}{L_{\sigma vFr}} = 2.9\, f_w(Fr, x)\, x^{-1.49}, \qquad 2.25 \leq x \leq \frac{3}{2}Fr, \tag{A6}$$

$${\rho'}_{oFr} = 0.056\, f_{\rho'}(Fr)\, x^{17.5Fr^{-1}}, \qquad 2.25 \leq x \lesssim \frac{3}{2}Fr, \tag{A7}$$

$$f_v(Fr) = 0.26 \tanh\left(0.39\frac{Fr}{2}\right),$$
$$f_w(Fr, x) = 0.15\left[2 + \sin\left(1.16\frac{\pi}{2}\left(\frac{2\,x}{Fr}\right)^{0.94}\right)\right],$$
$$f_{\rho'}(Fr) = \tanh\left(\frac{Fr}{6}\right)\exp\left(-15Fr^{-2}\right).$$

Step 3. Use centerline values from Step 2 to calculate $U(x, y, z)$, $u'(x, y, z)$, $v'(x, y, z)$, $w'(x, y, z)$, and $\rho'(x, y, z)$ by using (or interpolating) the coefficients from Tables II and III along

with the form of Eqs. (51) and (52) to complete the spatially varying flow field,

$$\left.\frac{q(x,z)}{q_o(x)}\right|_{Fr} = \exp\left[-\frac{(z/L_{\sigma v}-B_z)^2}{C_z^2}+\frac{B_z^2}{C_z^2}\right]+\exp\left[-\frac{(z/L_{\sigma v}+B_z)^2}{C_z^2}+\frac{B_z^2}{C_z^2}\right],$$

$$\left.\frac{q(x,y)}{q_o(x)}\right|_{Fr} = \exp\left[-\frac{(y/L_{\sigma h}-B_y)^2}{C_y^2}+\frac{B_y^2}{C_y^2}\right]+\exp\left[-\frac{(y/L_{\sigma h}+B_y)^2}{C_y^2}+\frac{B_y^2}{C_y^2}\right].$$

Step 4. Complete any remaining standard simulation initialization procedures.

[1] P. Meunier and G. R. Spedding, "A loss of memory in stratified momentum wakes," Phys. Fluids **16**, 298–305 (2004).
[2] P. Meunier and G. R. Spedding, "Stratified propelled wakes," J. Fluid Mech. **552**, 229–256 (2006).
[3] G. R. Spedding, "The evolution of initially turbulent bluff-body wakes at high internal Froude number," J. Fluid Mech. **337**, 283–301 (1997).
[4] H. Hanazaki, "A numerical study of three-dimensional stratified flow past a sphere," J. Fluid Mech. **192**, 393–419 (1988).
[5] J. W. Rottman, K. A. Brucker, D. G. Dommermuth, and D. Broutman, "Parameterization of the near-field internal wave field generated by a submarine," in *28th Symposium on Naval Hydrodynamics, Pasadena, California, USA, 12–17 September 2010* (Office of Naval Research, Arlington, Virginia, 2010), p. 790.
[6] R. Pasquetti, "Temporal/spatial simulation of the stratified far wake of a sphere," Comput. Fluids **40**, 179–187 (2011).
[7] Y. T. Fung and S. W. Chang, "Surface and internal signatures of organized vortex motions in stratified fluids," Phys. Fluids **8**, 3023 (1996).
[8] M. J. Gourlay, S. C. Arendt, D. C. Fritts, and J. Werne, "Numerical modeling of initially turbulent wakes with net momentum," Phys. Fluids **13**, 3783–3802 (2001).
[9] K. A. Brucker and S. Sarkar, "A comparative study of self-propelled and towed wakes in a stratified fluid," J. Fluid Mech. **652**, 373–404 (2010).
[10] D. G. Dommermuth, J. W. Rottman, G. E. Innis, and E. A. Novikov, "Numerical simulation of the wake of a towed sphere in a weakly stratified fluid," J. Fluid Mech. **473**, 83–101 (2002).
[11] P. J. Diamessis, J. A. Domaradzki, and J. S. Hesthaven, "A spectral multidomain penalty method model for the simulation of high Reynolds number localized incompressible stratified turbulence," J. Comput. Phys. **202**, 298–322 (2005).
[12] P. J. Diamessis, G. R. Spedding, and J. A. Domaradzki, "Similarity scaling and vorticity structure in high-Reynolds-number stably stratified turbulent wakes," J. Fluid Mech. **671**, 52–95 (2011).
[13] M. B. de Stadler, S. Sarkar, and K. A. Brucker, "Effect of the Prandtl number on a stratified turbulent wake," Phys. Fluids **22**, 095102 (2010).
[14] T. S. Orr, "Numerical simulations of linearly stratified flow around a sphere," Ph.D. thesis (University of Southern California, 2014).
[15] P. J. Stockhausen, C. B. Clark, and J. F. Kennedy, "Three-dimensional momentumless wakes in density-stratified liquids," Technical Report No. 93, Hydrodynamics Laboratory, Department of Civil Engineering, Massachusetts Institute of Technology, 1966.
[16] P. Bonneton, J. M. Chomaz, E. J. Hopfinger, and M. Perrier, "The structure of the turbulent wake and the random internal wave field generated by a moving sphere in a stratified fluid," Dyn. Atmos. Oceans **23**, 299–308 (1996).
[17] T. Sarpkaya and T. Massidda, "Conductivity measurements in the wake of submerged bodies in density-stratified media," in *Twenty-First Symposium on Naval Hydrodynamics* (National Academies Press, Washington, DC, 1997), pp. 266–277.
[18] M. Bonnier, O. Eiff, and P. Bonneton, "On the density structure of far-wake vortices in a stratified fluid," Dyn. Atmos. Oceans **31**, 117–137 (2000).
[19] G. R. Spedding, F. K. Browand, and A. M. Fincham, "Turbulence, similarity scaling and vortex geometry in the wake of a towed sphere in a stably stratified fluid," J. Fluid Mech. **314**, 53–103 (1996).
[20] E. J. Hopfinger, J.-B. Flor, J.-M. Comaz, and P. Bonneton, "Internal waves generated by a moving sphere and its wake in a stratified fluid," Exp. Fluids **11**, 255–261 (1991).
[21] P. Bonneton, J. M. Chomaz, and E. J. Hopfinger, "Internal waves produced by the turbulent wake of a sphere moving horizontally in a stratified fluid," J. Fluid Mech. **254**, 23–40 (1993).
[22] G. S. Constantinescu and V. C. Patel, "Numerical model for simulation of pump-intake flow and vortices," J. Hydraul. Eng. **124**, 123–134 (1998).
[23] M. Koken and G. Constantinescu, "An investigation of the dynamics of coherent structures in a turbulent channel flow with a vertical sidewall obstruction," Phys. Fluids **21**, 085104 (2009).
[24] A. G. Tomboulides and S. A. Orszag, "Numerical investigation of transitional and weak turbulent flow past a sphere," J. Fluid Mech. **416**, 45–73 (2000).
[25] T. A. Johnson and V. C. Patel, "Flow past a sphere up to a Reynolds number of 300," J. Fluid Mech. **378**, 19–70 (1999).
[26] G. S. Constantinescu and K. D. Squires, "LES and DES investigations of turbulent flow over a sphere at Re = 10,000," Flow, Turbul. Combust. **70**, 267–298 (2003).
[27] G. S. Constantinescu, M. Chapelet, and K. Squires, "Turbulence modeling applied to flow over a sphere," AIAA J. **41**, 1733–1742 (2003).
[28] G. S. Constantinescu and K. Squires, "Numerical investigations of flow over a sphere in the subcritical and supercritical regimes," Phys. Fluids **16**, 1449–1466 (2004).
[29] D. J. Bodony, "Analysis of sponge zones for computational fluid mechanics," J. Comput. Phys. **212**, 681–702 (2006).
[30] R. Mittal, "A Fourier-Chebyshev spectral collocation method for simulating flow past spheres and spheroids," Int. J. Numer. Methods Fluids **30**, 921–937 (1999).
[31] S. Taneda, "Experimental investigation of the wake behind a sphere at low Reynolds numbers," J. Phys. Soc. Jpn. **11**, 1104–1108 (1956).

[32] S. Lee, "A numerical study of the unsteady wake behind a sphere in a uniform flow at moderate Reynolds numbers," Comput. Fluids **29**, 639–667 (2000).
[33] J.-S. Wu and G. M. Faeth, "Sphere wakes in still surroundings at intermediate Reynolds numbers," AIAA J. **31**, 1448–1455 (1993).
[34] H. Sakamoto and H. Haniu, "A study on vortex shedding from spheres in a uniform flow," J. Fluids Eng. **112**, 386–392 (1990).
[35] F. Roos and W. Willmarth, "Some experimental results on sphere and disk drag," AIAA J. **9**, 285–291 (1971).
[36] H. J. Kim and P. A. Durbin, "Observations of the frequencies in a sphere wake and of drag increase by acoustic excitation," Phys. Fluids **31**, 3260–3265 (1988).
[37] Q. Lin, D. L. Boyer, and H. J. S. Fernando, "Turbulent wakes of linearly stratified flow past a sphere," Phys. Fluids A **4**, 1687–1696 (1992).
[38] J. A. Domaradzki and S. Radhakrishnan, "Effective eddy viscosities in implicit modeling of decaying high Reynolds number turbulence with and without rotation," Fluid Dyn. Res. **36**, 385–406 (2005).
[39] J. M. Chomaz, P. Bonneton, and E. J. Hopfinger, "The structure of the near wake of a sphere moving horizontally in a stratified fluid," J. Fluid Mech. **254**, 1–21 (1993).
[40] K. E. Lofquist and L. P. Purtell, "Drag on a sphere moving horizontally through a stratified liquid," J. Fluid Mech. **148**, 271–284 (1984).
[41] M. D. Greeslade, "Drag on a sphere moving horizontally in a stratified liquid," J. Fluid Mech. **418**, 339–350 (2000).
[42] B. Voisin, "Lee waves from a sphere in a stratified flow," J. Fluid Mech. **574**, 273–315 (2007).
[43] P. W. M. Brighton, "Strongly stratified flow past three-dimensional obstacles," Q. J. R. Meteorol. Soc. **104**, 289–307 (1978).
[44] G. R. Spedding, "Anisotropy in turbulence profiles of stratified wakes," Phys. Fluids **13**, 2361–2372 (2001).
[45] G. R. Spedding, "Vertical structure in stratified wakes with high initial Froude number," J. Fluid Mech. **454**, 71–112 (2002).
[46] J. Lighthill, *Waves in Fluids* (Cambridge University Press, New York, NY, 1978).
[47] J. Jeong and F. Hussain, "On the identification of a vortex," J. Fluid Mech. **285**, 69–94 (1995).
[48] M. Bonnier and O. Eiff, "Experimental investigation of the collapse of a turbulent wake in a stably stratified fluid," Phys. Fluids **14**, 791–801 (2002).